Impact of Ground-Based Remote Sensing Boundary Layer Observations on Short-Term Probabilistic Forecasts of a Tornadic Supercell Event

JUNJUN HU

Cooperative Institute for Mesoscale Meteorological Studies, University of Oklahoma, and NOAA/OAR/National Severe Storms Laboratory, Norman, Oklahoma

NUSRAT YUSSOUF

Cooperative Institute for Mesoscale Meteorological Studies, University of Oklahoma, and NOAA/OAR/National Severe Storms Laboratory, and School of Meteorology, University of Oklahoma, Norman, Oklahoma

DAVID D. TURNER

NOAA/OAR/Earth System Research Laboratory/Global Systems Division, Boulder, Colorado

THOMAS A. JONES

Cooperative Institute for Mesoscale Meteorological Studies, University of Oklahoma, and NOAA/OAR/National Severe Storms Laboratory, Norman, Oklahoma

XUGUANG WANG

School of Meteorology, University of Oklahoma, Norman, Oklahoma

(Manuscript received 20 December 2018, in final form 24 July 2019)

ABSTRACT

Due to lack of high spatial and temporal resolution boundary layer (BL) observations, the rapid changes in the near-storm environment are not well represented in current convective-scale numerical models. Better representation of the near-storm environment in model initial conditions will likely further improve the forecasts of severe convective weather. This study investigates the impact of assimilating high temporal resolution BL retrievals from two ground-based remote sensing instruments for short-term forecasts of a tornadic supercell event on 13 July 2015 during the Plains Elevated Convection At Night field campaign. The instruments are the Atmospheric Emitted Radiance Interferometer (AERI) that retrieves thermodynamic profiles and the Doppler lidar (DL) that measures horizontal wind profiles. Six sets of convective-scale ensemble data assimilation (DA) experiments are performed: two control experiments that assimilate conventional and WSR-88D radar observations using either relaxation-to-prior-spread (RTPS) or the adaptive inflation (AI) technique and four experiments similar to the control but that assimilate either DL or AERI or both observations in addition to all other observations that are in the control experiments. Results indicate a positive impact of AERI and DL observations in forecasting convective initiation (CI) and early evolution of the supercell storm. The experiment that employs the AI technique to assimilate BL observations in DA enhances the humidity in the near-storm environment and low-level convergence, which in turn helps forecasting CI. The forecast improvement is most pronounced during the first ~3 h. Results also indicate that the AERI observations have a larger impact compared to DL in predicting CI.

1. Introduction

Significant improvements in severe weather forecasting have been achieved during the past decade through assimilation of meso- and convective-scale observations from in situ and remote sensing instruments into convection-scale numerical weather prediction (NWP) models. These include assimilation of surface observations from instruments like automated surface observing systems and mesonets (e.g., Fujita et al. 2007;

Corresponding author: Junjun Hu, junjun.hu@noaa.gov

DOI: 10.1175/WAF-D-18-0200.1

Knopfmeier and Stensrud 2013; Sobash and Stensrud 2015), upper-air observations from radiosondes, dropsondes, Aircraft Communications Addressing and Reporting Systems (ACARS; e.g., Coniglio et al. 2016; Hitchcock et al. 2016), Weather Surveillance Radar-1988 Doppler (WSR-88D) Doppler velocity and reflectivity (e.g., Snyder and Zhang 2003; Dowell et al. 2004; Gao and Stensrud 2012; Yussouf et al. 2013, 2015; Johnson et al. 2015; Wang and Wang 2017), satellite measurements (e.g., Jones and Stensrud 2012; Jones et al. 2018; Polkinghorne and Vukicevic 2011), and all available observations from these instrument types (e.g., Zhang et al. 2006; Snook et al. 2011; Romine et al. 2013; Stensrud et al. 2013; Johnson et al. 2015; Wheatley et al. 2015; Jones et al. 2016). These observing platforms provide complementary information of the three-dimensional atmospheric states and assimilating these observations in NWP model improves the accuracy of model initial conditions and subsequent forecasts of convective weather.

However, despite significant progress in convective-scale modeling, predicting convection initiation (CI) remains a significant challenge (Kain et al. 2013 and references therein). CI is triggered by a variety of forcing mechanisms, such as cold fronts, drylines, gust fronts, gravity waves, outflow boundaries, topographically induced boundaries, convective rolls as well as their intersections (Weckwerth and Parsons 2006 and references therein). The current state-of-the-art convective-scale models have little skill in forecasting CI mainly due to deficiencies such as systematic biases in planetary boundary layer (BL) parameterization schemes, inadequate grid spacing to resolve the storm-scale processes that modulate CI, and the lack of adequate observations at high spatial and temporal resolution, in particular, through the depth of the BL (Coniglio et al. 2013; Romine et al. 2013; Sobash and Stensrud 2015).

Several studies have investigated the impact of assimilating nontraditional observations on forecasting CI. For example, Xue and Martin (2006) showed that the assimilation of special upper-air and surface observations that are not routinely available improved the accuracy of CI of a convective event. More recently, Sobash and Stensrud (2015) demonstrated the assimilation of surface mesonet observations in improving the forecast of dryline location and subsequent convective evolution. Degelia et al. (2018) explored the impact of assimilating radar and routinely available in situ observations on a summer nocturnal CI event on 25 June 2013. Those studies suggest that an accurate representation of the rapidly evolving storm and near-storm environment in model initial conditions is crucial for forecasting CI. Therefore, exploring emerging nontraditional thermodynamic and kinematic observing platforms sensitive to the lowest few kilometers of the atmosphere, and assimilating those BL observations into convective-scale NWP model is a worthwhile effort.

The National Research Council (NRC) issued two reports concerning the development of mesoscale meteorological observational capabilities (NRC 2009) and the priorities on U.S. weather research and research-to-operation activities (NRC 2010). Both reports strongly recommended a network of ground-based thermodynamic and kinematic profilers to sample the BL, in particular the lowest 2–3 km of the atmosphere. One such instrument is the Atmospheric Emitted Radiance Interferometer (AERI), which provides thermodynamic profiles (Hoff and Hardesty 2012; Turner and Löhnert 2014) of the BL. The AERI retrievals are used in various applications, such as for recording the thermodynamic evolution of BL (Feltz et al. 1998; Turner et al. 2000), monitoring preconvective environment evolution (Feltz and Mecikalski 2002), and differentiating convective indices between tornadic and nontornadic storms (Wagner et al. 2008). Another instrument that complements AERI is the Doppler lidar (DL), which measures the horizontal wind speed, direction, and vertical velocities (Newsom et al. 2017). The DLs have been used in applications such as atmospheric BL research (Chai et al. 2004; Newsom and Banta 2004a,b; Newsom et al. 2005) and significant wind shear detection (e.g., Shun and Chan 2008). The combination of AERI and DL instruments provides high-resolution measurements of BL thermodynamic and kinematic evolution and structure.

The AERI and DL have been used in various field campaigns to measure the evolution of BL near-storm environment. One such field campaign is the Plains Elevated Convection At Night (PECAN; Geerts et al. 2017) that took place from 1 June to 15 July 2015 over the U.S. Great Plains. The goal of the PECAN field campaign was to improve the understanding and simulation of processes that initiate and maintain night time convection. The field campaign's unique observational strategy included the concept of the PECAN Integrated Sounding Array (PISA), where each PISA site included thermodynamic and kinematic profilers together with surface meteorological observations. Six fixed PISA (FP) sites (Fig. 1c) were deployed and operated continuously during the PECAN field phase. AERI and DL were among the several instruments that were stationed at those PISA sites (all six sites had AERI but only four of them FP1, FP2, FP3, and FP6 had DL).

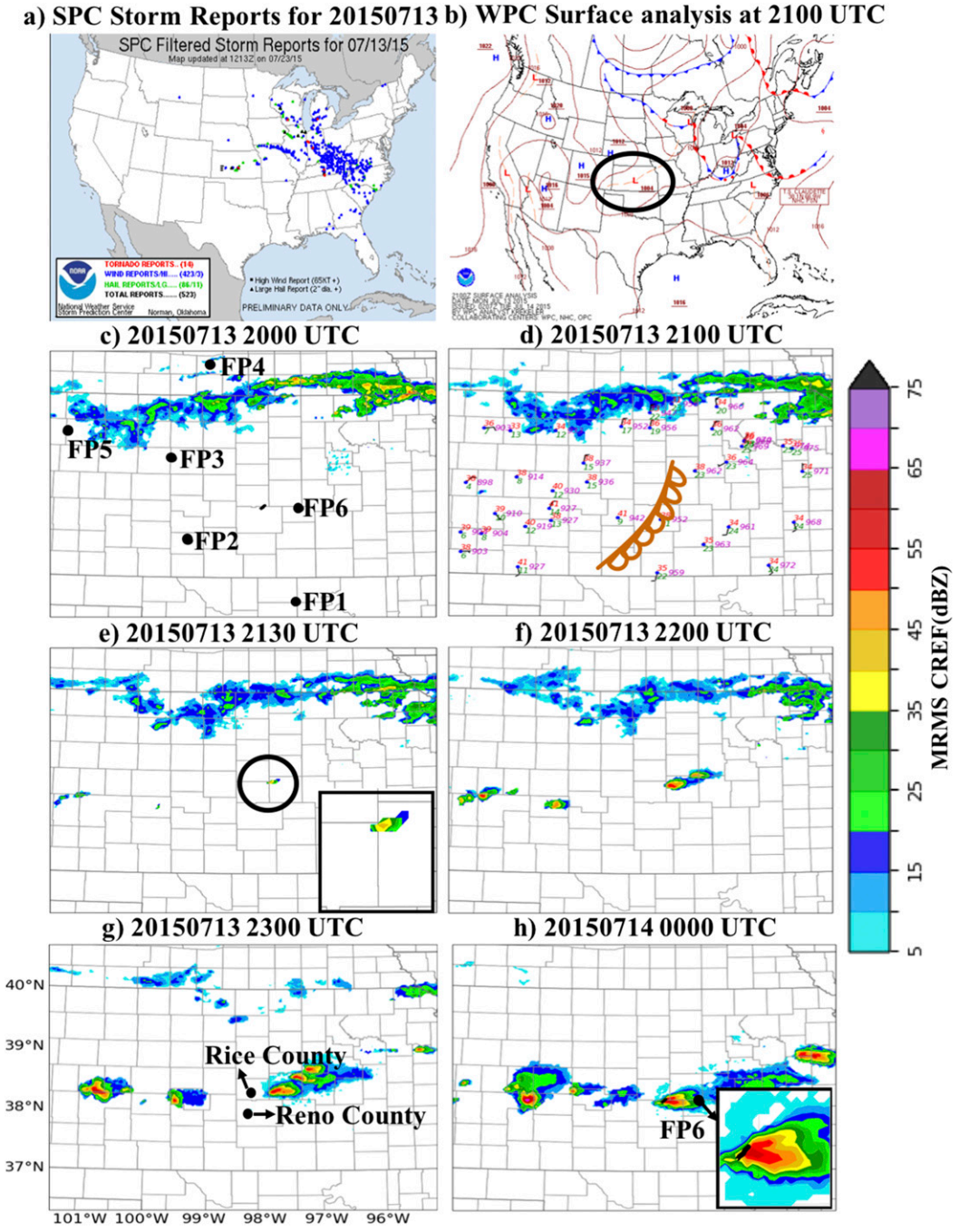

FIG. 1. (a) Severe storm reports for 13 Jul 2015 from the Storm Prediction Center (SPC). (b) Weather Prediction Center (WPC) surface analysis at 2100 UTC 13 Jul 2015; a pressure trough is located across the entire state of Kansas. MRMS CREF at (c) 2000 UTC with six FP stations shown in black dots, (d) 2100 UTC with Kansas mesonet surface observations (temperature in red, dewpoint temperature in green, pressure in purple, wind barbs in black, and weak dryline in brown), (e) 2130 UTC, (f) 2200 UTC, (g) 2300 UTC, and (h) 0000 UTC 14 Jul 2015 with the damage track of the Nickerson, KS, tornado overlaid in black.

Observations from numerous severe weather events were archived by the measuring platforms during the PECAN field campaign. One such event was a severe thunderstorm event producing an EF3 tornado on 13 July 2015 near Nickerson, Kansas. The Storm Prediction Center highlighted the area as having the potential for isolated severe convection with straight-line winds being the primary threat. The lack of deep-level

surface moisture and large-scale convergence represented a potential limiting factor for severe weather, which resulted in the decision not to issue a watch. However, a significant tornado did occur from this environment indicating that smaller-scale features that may not have been obvious in existing observations or model forecasts played an important role. So, this study examines whether assimilating AERI and DL retrievals in convective-scale NWP will improve the retrospective prediction of this supercell event through better analyses of the near-storm environment. We utilize an ensemble-based probabilistic approach that is essential for convective-scale modeling as the uncertainties associated with severe weather prediction are highly due to large sensitivity of both environmental conditions and internal storm processes (Stensrud et al. 2013 and references therein). Unlike Coniglio et al. (2019), who showed the positive impact of assimilating AERI and DL profiles from a single station on the early evolution of thunderstorms using several severe weather days, this study focuses on a single case study and explore the impact of assimilating a network of AERI and DL profiles and the choice of the inflation techniques in convective-scale data assimilation (DA) configuration on short-term predictions of CI and early evolution of a tornadic supercell thunderstorm. The hypothesis of this study is that the assimilation of temperature, moisture, and horizontal wind variables from these ground-based sensors should improve the characterization of BL conditions in the model and hence improve the short-term forecasts of severe thunderstorm.

An overview of the tornadic event is presented in section 2. In section 3, we describe the AERI and DL instruments and preprocessing of the retrievals. Section 4 discusses the experimental design and the DA system configuration, and section 5 discusses the results obtained from experiments. Finally, section 6 provides a summary followed by final discussions.

2. Overview of the 13 July 2015 Nickerson tornadic supercell event

The Nickerson, Kansas, tornadic supercell event was the only tornado on 13 July 2015 (Fig. 1a) over the central contiguous United States (CONUS). In the afternoon, the surface temperature was higher than 35°C and the dewpoint depression was larger than 10°C (Fig. 1d), which resulted in high cloud bases with lifting condensation levels higher than 1.5 km above the surface. However, a few widely separated thunderstorms developed across central Kansas during the late afternoon (Figs. 1e–h and 2). The Nickerson tornadic supercell storm initiated at the intersection of a pressure trough and a weak dryline (Figs. 1b,d) across central Kansas between 2100 and 2130 UTC (Figs. 1e and 2b). The storm was initiated on the moist side of the dryline and then moved slowly south-southwest across part of Rice and Reno counties and produced a large EF3 tornado near Nickerson, Kansas. The tornado touched down at around 2335 UTC and moved southwest during the next 20 min (Fig. 1h). The AERI and DL instruments stationed at the FP sites operated 24 h a day and provided near continuous thermodynamic and kinematic BL profile measurements of the environment, making this a good case study to evaluate the impact of AERI and DL in forecasting the supercell event.

3. Description of the ground-based remote sensing boundary layer instruments

a. Atmospheric Emitted Radiance Interferometer

The AERI is a ground-based passive remote sensing instrument that employs a Fourier transform spectrometer to measure the downwelling infrared radiance emitted from the atmosphere. It was designed for the U.S. Department of Energy Atmospheric Radiation Measurement (ARM) Program by the University of Wisconsin Space Science and Engineering Center in the 1990s (Stokes and Schwartz 1994; Turner et al. 2016). Since then, the deployment of AERI has been extended worldwide. The spectrometer operates in a broad spectral range (3.3–19.2 μm) with sufficient spectral resolution (about 1 cm^{-1}) to discriminate between suspended matter (e.g., aerosols, water droplets, and ice crystals) and gaseous emitters (e.g., carbon dioxide and water vapor). From AERI-observed radiance data, vertical profiles of tropospheric temperature and water vapor mixing ratio can be retrieved using the AERIoe algorithm (Turner and Löhnert 2014; Turner and Blumberg 2019). AERIoe is an iterative retrieval method that starts with a first guess of the temperature and humidity profiles and uses the ''line-by-line radiative transfer'' forward model to compute simulated AERI radiance observations from these profiles. (The retrieved solution from AERIoe is relatively insensitive to the actual first guess used, and for our application here we used the climatological mean profile as the first guess.) AERIoe propagates the uncertainty in the observations and the sensitivity of the forward model to provide a full error covariance matrix of the retrieved profiles (further details about AERIoe in Turner and Löhnert 2014). The $1 - \sigma$ uncertainty, which is the square root of the diagonal of the error covariance matrix, provides a simple way to look at the

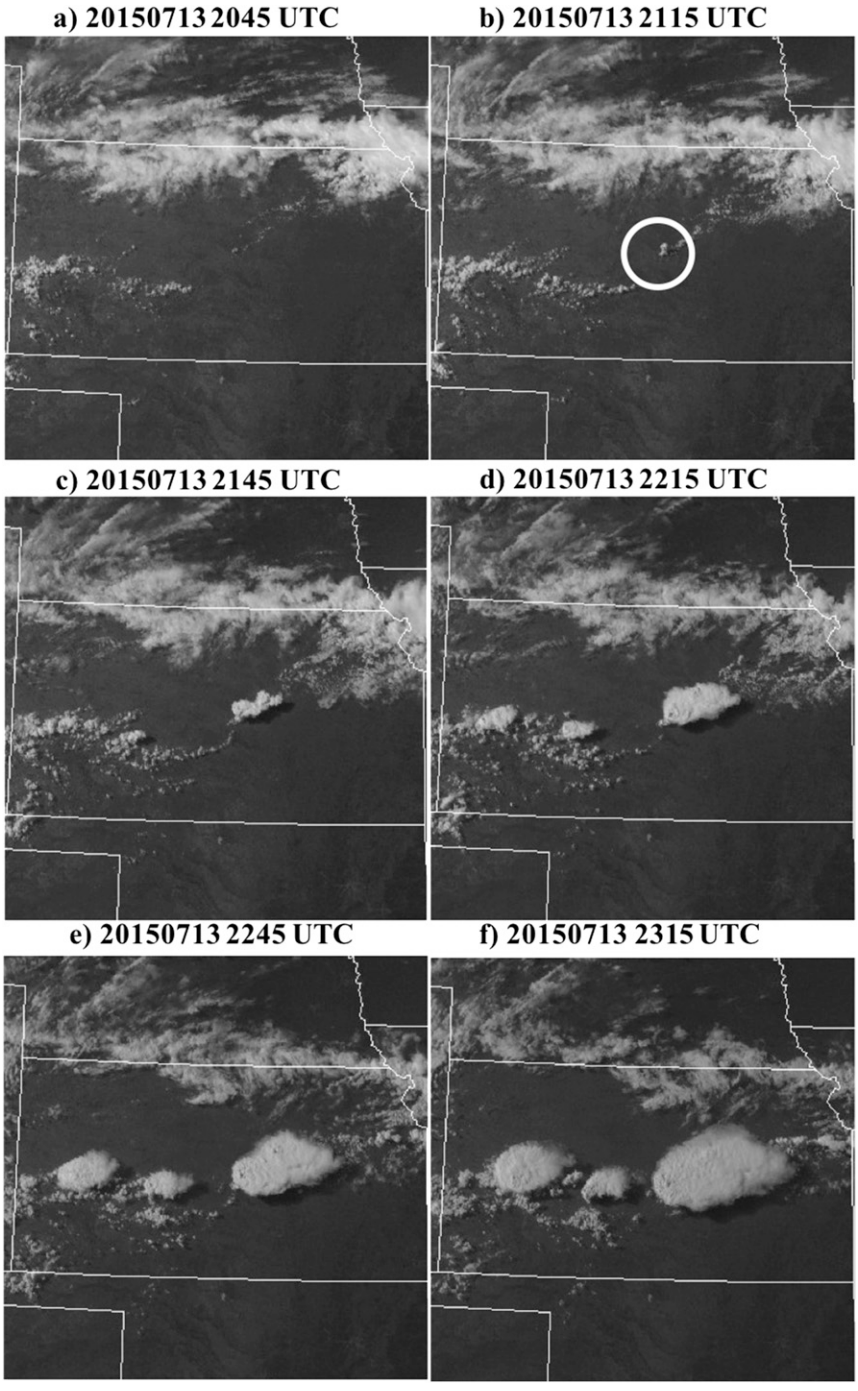

FIG. 2. Visible satellite images from *GOES-13* at (a) 2045, (b) 2115, (c) 2145, (d) 2215, (e) 2245, and (f) 2315 UTC 13 Jul 2015. The white circle in (b) denotes the area of CI.

uncertainty of the retrieval as a function of height. During the PECAN field campaign, the AERIs deployed at each FP station retrieved thermodynamic profiles every 5 min from the ground through the top of the BL or cloud-base height (CBH), which ever was lower. On average, the vertical resolution was approximately the same as the altitude of the observation (e.g., the retrieval has 1-km vertical resolution at 1 km AGL; Turner and Löhnert 2014). However, Turner and Löhnert (2014) also shows that the information content (and hence vertical resolution) changes with water vapor in the planetary BL.

b. Doppler lidar

The DL is an active remote sensing instrument. It transmits short pulses of infrared laser light into the atmosphere and a small fraction of that light energy is scattered back by atmospheric aerosols, which are ideal tracers of atmospheric wind fields. The radial air velocity is analyzed using the Doppler frequency shift imparted on the backscatter signal (Pearson et al. 2009). The DL performs a plan position indicator (PPI) scan at different azimuthal angles and horizontal wind speed and direction are derived from the radial velocity using the velocity azimuth display (VAD) technique (Klein et al. 2015). Valid measurements from the DL are usually limited to BL where aerosol concentrations are high. The kinematic profiles are retrieved approximately every 5 min, and the vertical resolution of the horizontal wind profile is about 30 m.

c. Observation preprocessing

Simple quality control (QC) is performed before assimilating the AERI and DL measurements into the model. For DL, the observed PPI radial velocities are fit using a sine wave (in the standard VAD approach) and root mean squared error (RMSE) values between observed PPI radial velocities and fitted values are calculated. Any levels with RMSE greater than 0.5 m s^{-1} are disregarded. Several criteria are taken into consideration to QC the AERI retrievals. First, the observations above CBH are ignored where the liquid water path is over 6.0 g m^{-2} (Blumberg et al. 2015). Second, if the $1-\sigma$ uncertainty of temperature is greater than 1.0°C or the $1-\sigma$ uncertainty of water vapor mixing ratio is greater than 1.5 g kg^{-1}at the lowest level, then the whole column is disregarded. Finally, only retrievals that converged and have an RMSE between the observed and predicted (from the forward model) radiance less than the predefined threshold (unitless; 30.0 for FP1, 5.0 for FP6, and 10.0 for other stations) are used. The FP6 site located at Hesston, Kansas, was within the storm inflow region of the tornadic supercell throughout its life cycle (Fig. 1h). The time–height plot from site FP6 indicates a strong nocturnal inversion mixed out after sunrise that enabled deep mixing (Fig. 3a). The weak dryline and the convergence along the pressure trough (Figs. 1b,d) provided enough lift for parcels to reach the level of free convection (LFC), and the storm initiated at the intersection of the trough and dryline. The discontinuity of the data (white pixels in Fig. 3) during later time of the day are the missing or noisy values that are removed during QC. On 13 July 2015, there was an increase in the water vapor in the planetary BL, therefore the vertical resolution is higher than the average value discussed in Turner and Löhnert (2014).

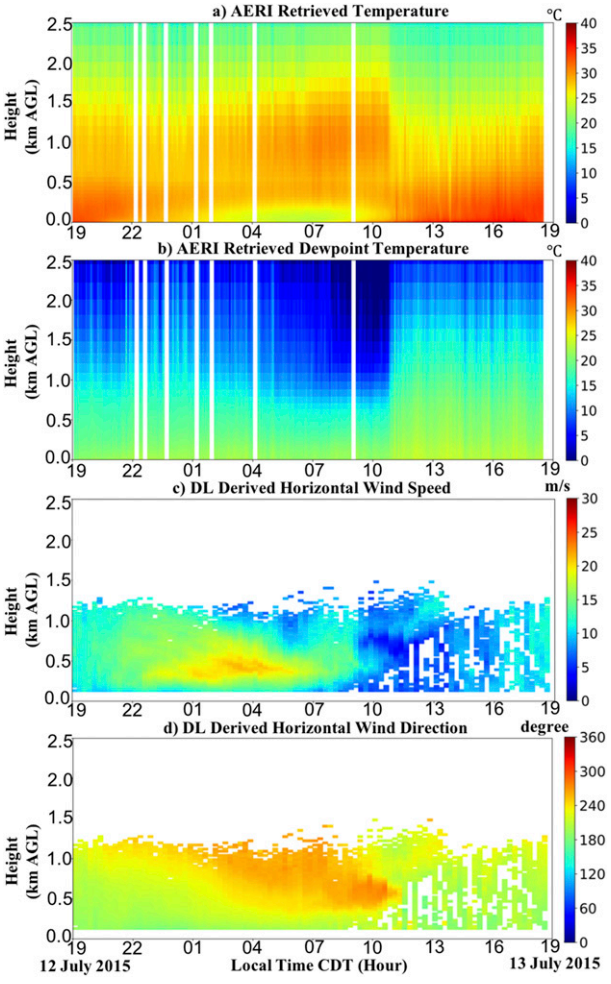

FIG. 3. Time–height diagram of (a) temperature, (b) dewpoint temperature retrievals from AERI, and (c) horizontal wind speed and (d) horizontal wind direction retrieved from DL on 12–13 Jul 2015 at station FP6. White areas represent missing or noisy data after quality control.

The high-resolution AERI and DL retrievals in the vertical are thinned to help reduce both the correlated and uncorrelated error in observation (Berger and Forsythe 2004; Ochotta et al. 2005). For AERI, measurements at vertical levels 50, 100, 150, 200, 300, 400, 500, 600, 700, 800, 900, 1000, 1100, 1200, 1300, 1400, 1500, 1750, and 2000 m AGL are selected. Likewise, for DL, measurements at vertical levels 100, 200, 300, 400, 500, 600, 700, 800, 900, 1000, 1100, 1200, 1300, 1400, 1500, 1750, and 2000 m AGL are utilized.

4. Experiment design

a. The multiscale WRF ensemble and DA system

The configuration of the multiscale ensemble DA and prediction system is very similar to that used in

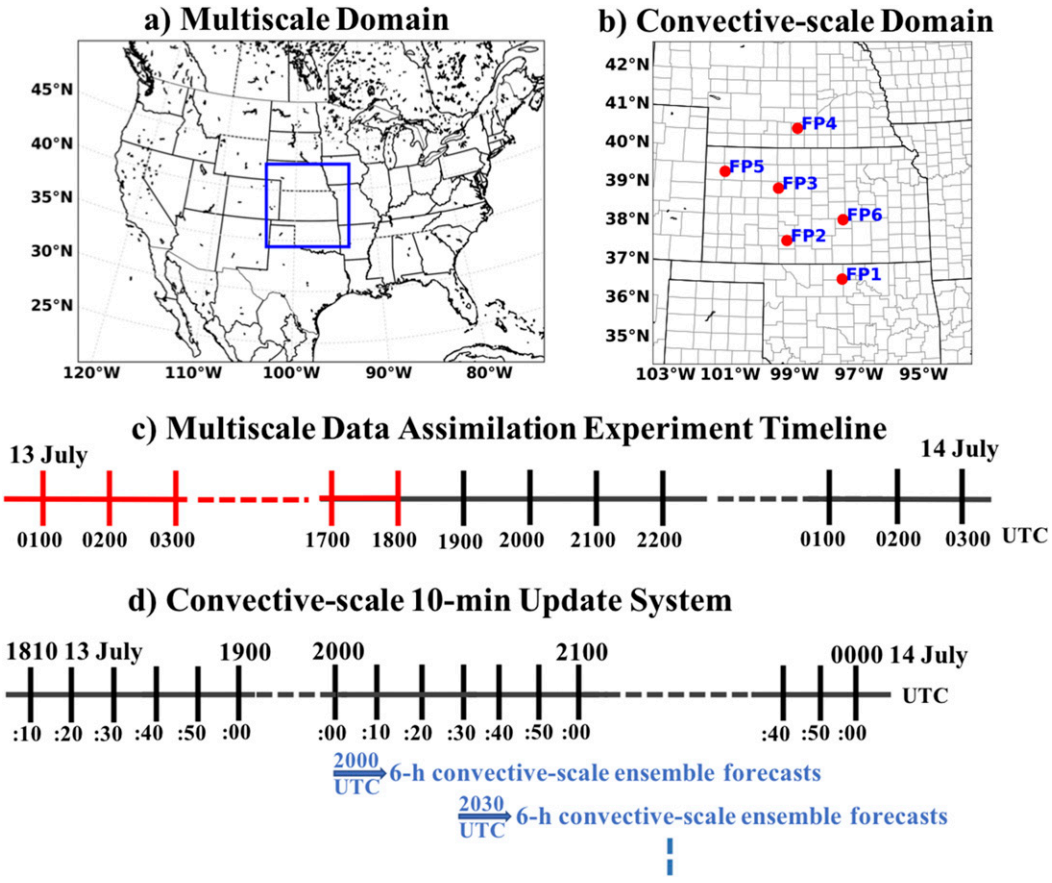

FIG. 4. (a) The multiscale domain with the 15-km horizontal grid-spacing mesoscale domain covering the CONUS and the nested 3-km convective-scale domain centered over the entire state of Kansas. (b) The convective-scale domain enlarged with six FP sites from the PECAN field campaign. (c) The timeline of the hourly multiscale DA experiments. Starting from 1900 UTC, only the mesoscale (15 km) domain is cycled hourly. (d) The timeline for the 10-min convective-scale DA experiments.

Yussouf et al. (2015, 2016). The Advanced Research version of the Weather Research and Forecasting (WRF-ARW, version 3.8.1; Skamarock et al. 2008) Model is used for this study with a parent mesoscale domain (with grid spacing of 15 km) over the contiguous United States (Fig. 4a) and a convective-scale domain (with grid spacing of 3 km) nested within the mesoscale domain that covers Kansas and parts of the surrounding states (Fig. 4b). There are 51 vertical grid levels ranging from the surface to 10 hPa on the top. A 36-member multiphysics ensemble is initialized at 0000 UTC 13 July 2015 using the analyses from National Centers for Environmental Prediction's (NCEP) Global Ensemble Forecasting System (GEFS; Toth et al. 2004; Wei et al. 2008; Zhou et al. 2016). The ensemble system is created using different combinations of physics and radiation schemes and is very similar to that in Table 2 of Yussouf et al. (2015) and Wheatley et al. (2015). GEFS also provides boundary conditions for the 15-km domain.

This study uses the Gridpoint Statistical Interpolation (GSI; Hu et al. 2017b; Kleist et al. 2009)-based ensemble Kalman filter (EnKF; Whitaker and Hamill 2002; Whitaker et al. 2008; Liu et al. 2017) DA system (GSI-EnKF). The GSI-EnKF is used as a component within the NCEP operational hybrid DA for both global prediction (Wang et al. 2013) and convection allowing hurricane prediction (Lu et al. 2017a,b). GSI-EnKF is also used as part of the North American Mesoscale Forecast System (NAM) and Rapid Refresh (RAP) systems (Hu et al. 2017a; Wu et al. 2017). After GSI was transitioned into a community-based code (Shao et al. 2016), the research community began to expand the system for regional mesoscale and convective-scale DA and predictions (e.g., Pagowski and Grell 2012; Johnson et al. 2015, Schwartz 2016; Wang and Wang 2017; Wu et al. 2017; Hu et al. 2017a).

The GSI component of the DA system performs an outlier check to the observations, interpolates the model

TABLE 1. The list of instruments, variables assimilated, and the covariance localization length scale (where hloc and vloc refer to horizontal and vertical localization, respectively) used in this study.

Observations	hloc (km)	vloc [$\ln(p/p_{ref})$]	Variables
Conventional	460	0.45	T, T_d, u and v wind, P_s
Oklahoma mesonet	60	0.45	T, T_d, u and v wind, P_s
Radar	18	0.80	Reflectivity, radial velocity
AERI	400	0.45	T and T_d
DL	400	0.45	u and v wind

first-guess fields to observation space and then calculates the innovation (observation − background). If the ratio of the innovation to the observation error is greater than a certain threshold, that observation is rejected ("convinfo" file in Hu et al. 2017b). In addition to the outlier check in GSI, which is only a function of observation error, the EnKF performs an outlier check that additionally incorporates ensemble spread. Assuming a threshold sprd_tol, if the difference between an observation O and those from the prior (forecast background or first guess F) mean $(O - F)$ is greater than sprd_tol $\times \sqrt{S + R}$, where S is ensemble prior variance and R is observation error variance, that observation is rejected (Liu et al. 2017). Similar to other convective-scale ensemble DA studies (Wheatley et al. 2015; Yussouf et al. 2015; Liu et al. 2017), a sprd_tol value 3.25 is used in this study. The fifth-order Gaspari–Cohn (Gaspari and Cohn 1999) localization function (Table 1) is used to eliminate spurious covariance due to sampling errors from limited ensemble size (Houtekamer and Zhang 2016).

To account for the ensemble underdispersion due to unrepresented systematic errors, the EnKF system in the GSI framework includes the relaxation to prior spread (RTPS; Whitaker and Hamill 2012) multiplicative covariance inflation technique. Suppose σ^b and σ^a are the prior and posterior ensemble spread (standard deviation) at each analysis grid point, RTPS relaxes the ensemble spread back to the prior via

$$\sigma^a \leftarrow (1 - \alpha)\sigma^a + \alpha\sigma^b \tag{1}$$

where α is a fraction parameter. If $\alpha = 1$, ensemble is inflated to make the posterior spread equal to the prior spread; If $\alpha = 0$, it indicates no inflation (Whitaker and Hamill 2012). Several recent studies use the RTPS inflation technique in regional multiscale cycled ensemble DA studies (Johnson et al. 2015, 2018; Schwartz and Liu 2014; Schwartz 2016; Wang and Wang 2017). Another variant of the inflation technique that is widely used in regional multiscale cycled ensemble DA studies (e.g., Schwartz et al. 2015; Sobash and Stensrud 2015; Wheatley et al. 2015; Yussouf et al. 2015, 2016; Jones et al. 2016) is the spatially and temporally varying multiplicative adaptive inflation (AI; Anderson 2009). In an effort to maintain the ensemble spread, AI is applied prior to applying the observation operators. We implemented the AI technique from National Center for Atmospheric Research's (NCAR) Data Assimilation Research Testbed (DART; Anderson and Collins 2007; https://www.image.ucar.edu/DAReS/DART; Anderson 2009) into the GSI-EnKF DA system. In AI, an inflation factor from the normal distribution is assigned to each element in the model state vector and the inflation factor is updated adaptively during each DA step using a Bayesian algorithm (Anderson 2009). The values of the inflation factors are estimated using the same observations that are used to update the state variables. The Gaussian mean and standard deviation of the inflation factor are initialized during the first DA cycle and used to generate the inflated prior ensemble. The inflated prior ensemble and the ensemble mean are then ingested into GSI system to compute the innovations. The EnKF updates the inflated prior ensemble as well as the mean and standard deviation of the inflation factor based on the innovations. The updated inflation values are used during the next DA cycle. For computational reasons, the inflation standard deviation are kept unchanged during the update (Anderson 2009).

b. *Continuous 1-h cycled multiscale ensemble DA*

The mesoscale and convective-scale domains are run concurrently in a one-way nest setup (following Yussouf et al. 2015) and cycled hourly for a 18-h period starting from 0100 UTC 13 July to 1800 UTC 13 July (Figs. 4a,c) and then only the 15-km domain from 1900 UTC 13 July to 0300 UTC 14 July using GSI-EnKF technique. Routinely available traditional observations from NCEP's PrepBUFR (World Meteorological Organization format) files are assimilated, which include pressure, temperature, moisture, and wind from rawinsondes, surface and marine stations, ACARS, AIREP/PIREP aircraft reports, Next Generation Weather Radar (NEXRAD) VAD wind reports, and profilers and Oklahoma mesonet observations. The error table defined for NAM from the GSI-EnKF system is used for the observation errors of observations included in PrepBUFR. The observation errors for temperature, dewpoint temperature, horizontal winds and surface pressure are 1.0 K, 1.0 K, 1.0 m s^{-1}, and 0.75 hPa, respectively, for Oklahoma mesonet data. The experiment is built on previous work that demonstrated the ability of a partially cycled EnKF DA to incorporate realistic mesoscale characteristics that often play an important role in

TABLE 2. The left column lists the name of the experiments in this study. The middle columns show the observation platforms assimilated, and the right column lists the inflation techniques used in each of the experiments.

Experiments	Observation					Inflation method
	Conventional	Oklahoma mesonet	Radar	AERI	DL	
CNTL_RTPS	Y	Y	Y	N	N	RTPS
CNTL_AI	Y	Y	Y	N	N	AI
AERI_DL_RTPS	Y	Y	Y	Y	Y	RTPS
AERI_DL_AI	Y	Y	Y	Y	Y	AI
AERI_AI	Y	Y	Y	Y	N	AI
DL_AI	Y	Y	Y	N	Y	AI

the development of storm (Fujita et al. 2007; Stensrud et al. 2009; Wheatley et al. 2012; Ha and Snyder 2014; Schwartz et al. 2015). The hourly updated mesoscale domain provides the boundary condition for the convective-scale domain.

c. *Frequent 10-min cycled convective-scale ensemble DA*

As mentioned earlier, CI for the Nickerson supercell occurred between 2100 and 2130 UTC. To examine the predictability of CI in the ensemble system and subsequent convective development, the convective-scale domain is cycled every 10 min starting from 1810 UTC, which is ~3.5 h before the storm initiated, for a 6-h period out to 0000 UTC (Figs. 4b,d). The 10-min forecast from the updated 3-km domain at 1800 UTC 13 July in hourly multiscale DA provides the initial condition for the 10-min cycled convective-scale DA and the hourly updated 15-km domain provides boundary condition to the 10-min cycled convective-scale DA. In addition to WSR-88D reflectivity, radial velocity, PrepBUFR files and Oklahoma mesonet observations, the cycled DA system also assimilates AERI and DL retrievals from the FP stations. The Multi-Radar Multi-Sensor (MRMS) reflectivity observations (Smith et al. 2016) and WSR-88D Doppler radial velocity are analyzed to a 5-km grid. Values of reflectivity below 0 dBZ are set to 0 dBZ representing ''no precipitation'' and any reflectivity values greater than 0 dBZ and less than 20 dBZ are not assimilated to reduce the generation of noisy spurious convection in the model. When reflectivity is less than 10 dBZ, radial velocity observations are omitted. The observation errors of reflectivity and radial velocity are assumed 5 dBZ and 2.0 m s^{-1}, respectively (Yussouf et al. 2016).

Observation errors for AERI and DL retrievals are approximated by inflating the rawinsonde observations defined in NAM error table (Liu et al. 2017). The observation error in DA system approximates both the instrument error and the representativeness error (Geer and Bauer 2011). In this study, the representativeness error for AERI temperature profiles are approximated by subtracting 0.2 K from total observation error profiles of rawinsonde temperature. The representativeness error for DL wind profiles are approximated equal to the total observation error profiles of rawinsonde wind. The $1 - \sigma$ uncertainties in the retrievals of AERI and DL profiles are added to the representativeness error profiles to estimate the total observation error profiles for AERI temperature and DL wind profiles. The observation error profiles for AERI dewpoint temperature retrievals are estimated following Lin and Hubbard (2004).

Several sensitivity tests were conducted using different localization length scales for AERI and DL, and the horizontal (vertical) length scales of 400 km (0.45 scale height) are selected as a reasonable choice for the localization length scales (Table 1). To counteract ensemble underdispersion that arises from assimilating highly dense radar observations, the additive noise technique (Dowell and Wicker 2009; Sobash and Wicker 2015) also is applied at each DA cycle to temperature, humidity, and wind variables where observed reflectivity exceeds 35 dBZ and the difference from model simulated reflectivity is greater than 10 dBZ.

Six sets of convective-scale DA and forecast experiments are conducted in this study (Table 2). The control experiments assimilate traditional observations, Oklahoma mesonets, reflectivity and radial velocity during the DA cycles. The CNTL_RTPS experiment uses the RTPS inflation technique. Several tests were conducted using different α ranging from values less than 1 to values greater than 1 (Johnson et al. 2015; Wang and Wang 2017; Schwartz and Liu 2014; Schwartz 2016) and the results were very similar. For the CNTL_RTPS, we chose inflation factor, $\alpha = 1.12$ (Schwartz and Liu 2014; Schwartz 2016). CNTL_AI experiment uses the AI inflation technique to prior ensembles for maintaining the ensemble spread. The initial inflation value of 1.0, a fixed standard deviation of 0.6 and a damping factor of 0.9 is used for the AI (Sobash and Stensrud 2015). Another set of experiments assimilate AERI and DL retrievals in

addition to all observations that are assimilated in the control experiment. The AERI_DL_RTPS experiment applies the RTPS inflation technique with $\alpha = 1.12$ as in CNTL_RTPS, and the AERI_DL_AI experiment applies adaptive prior multiplicative inflation technique with the same settings as in CNTL_AI. Finally, two additional experiments, namely, the AERI_AI and DL_AI experiments are conducted to examine which observing platform has the larger impact on the ensemble forecasts. The AERI_AI experiment assimilates AERI retrievals in addition to all observations that are assimilated in the control experiment and DL_AI assimilates DL retrievals as well as all observations assimilated in the control experiment. The 0–6-h ensemble forecasts using all 36 members are initialized from each experiment every 30 min, starting from 2000 UTC to evaluate the impact of assimilating AERI and/or DL on forecasting the timing and location of storm initiation and subsequent storm evolution. The differences in the results from applying the two inflation techniques will illuminate the impact of inflation choices on the ensemble forecasts.

5. Results and discussion

a. Convective initiation

Following Sobash and Stensrud (2015), CI is defined both in model forecasts and in radar observed storms (MRMS reflectivity) as areas where composite reflectivity (CREF) is greater than 25 dBZ as an indication of convective development. The gridpoint-based probability of CREF exceeding a threshold of 25 dBZ (denoted as Prob_CREF25 hereafter) is calculated from the ensemble forecasts initialized at 2000 UTC (Fig. 5). The Nickerson supercell initiated around ~2115–2130 UTC and its early evolution is shown in Figs. 5a–c. Another incipient storm (denoted as storm2) also developed northeast of the Nickerson storm (Figs. 5a–c). The CNTL_RTPS and CNTL_AI experiments fail to initiate any of the two storms during the 2100–2200 UTC forecast period (Figs. 5d–i). The AERI_DL_RTPS experiment (Figs. 5j–l) fails to initiate the Nickerson storm during the 2100–2200 UTC, but initiates storm2 at 2200 UTC, although it is displaced to the north (Fig. 5l). In contrast, there is an early sign of CI for the Nickerson storm (Fig. 5m) in AERI_DL_AI experiment with 10% probability at 2100 UTC, and the value increases to above 30% during the next 30 min (Fig. 5n). The probabilities increases to 50% at 2200 UTC (Fig. 5o). The forecast CI location of the Nickerson storm is slightly southeast from the observed location. Similar to AERI_DL_RTPS, the AERI_DL_AI experiment also predicts the initiation of storm2 with a northward bias, but with a higher probability (Figs. 5n–o). Clearly, the addition of AERI and DL observations in AERI_DL_AI experiment shows potential with forecasting the CI.

As mentioned earlier, the RTPS inflation technique aims at recovering the variance in the posterior analysis back to the prior. For a given value of α, the inflation is proportional to ensemble spread reduction caused by the assimilation of observations, normalized by the ensemble spread in the posterior (Whitaker and Hamill 2012; Liu et al. 2017). Therefore, locations with denser or larger impact observations have larger inflation. Conversely, each state elements in the AI technique has a normally distributed, spatially and temporally varying inflation factor that are adjusted based on a Bayesian algorithm (Anderson 2009; Hodyss et al. 2016) when updating the state. The same observations are used to update both the state and the inflation factor and therefore, larger adjustments are made in regions where dense and/or large impact observations are available (Anderson 2009). The differences in the ensemble spread at 2000 UTC right before calling the GSI component in experiments AERI_DL_RTPS and AERI_DL_AI are shown in Fig. 6. Compared to the AERI_DL_RTPS, the AERI_DL_AI experiment maintains a larger ensemble spread in near-storm environment for both temperature T and dewpoint temperature T_d (Figs. 6a,b) at 2000 UTC. AERI_DL_RTPS inflates the posterior analyses during the previous DA cycle at 1950 UTC, generates a 10-min forecast out to 2000 UTC and then the ensemble spread is calculated from the prior (or background). AERI_DL_AI generates a 10-min forecast using the analyses from 1950 UTC, inflates the forecast at 2000 UTC, and the ensemble spread is calculated after the inflation. With a larger ensemble spread, higher number of AERI T_d retrievals pass the outlier check and are assimilated in AERI_DL_AI especially during 1850–2000 UTC compared to that in AERI_DL_RTPS. Starting from 1930 UTC, all T_d retrievals are used to update the storm environment in AERI_DL_AI. Even though, both experiments assimilate the same number of T, u-wind, and v-wind retrievals (not shown), the AERI T_d plays a more significant role in storm initiation. Because of the more accurate CI forecasts from the AI inflation technique, the following sections will focus only on AERI_DL_AI and CNTL_AI experiments.

Not surprisingly, the ensemble mean reflectivity forecasts at 4 km above mean sea level (MSL; Fig. 7) also indicates that AERI_DL_AI initiates the Nickerson storm 60 min into forecast at around 2100 UTC (Fig. 7g). The cell starts to intensity with larger areal coverage

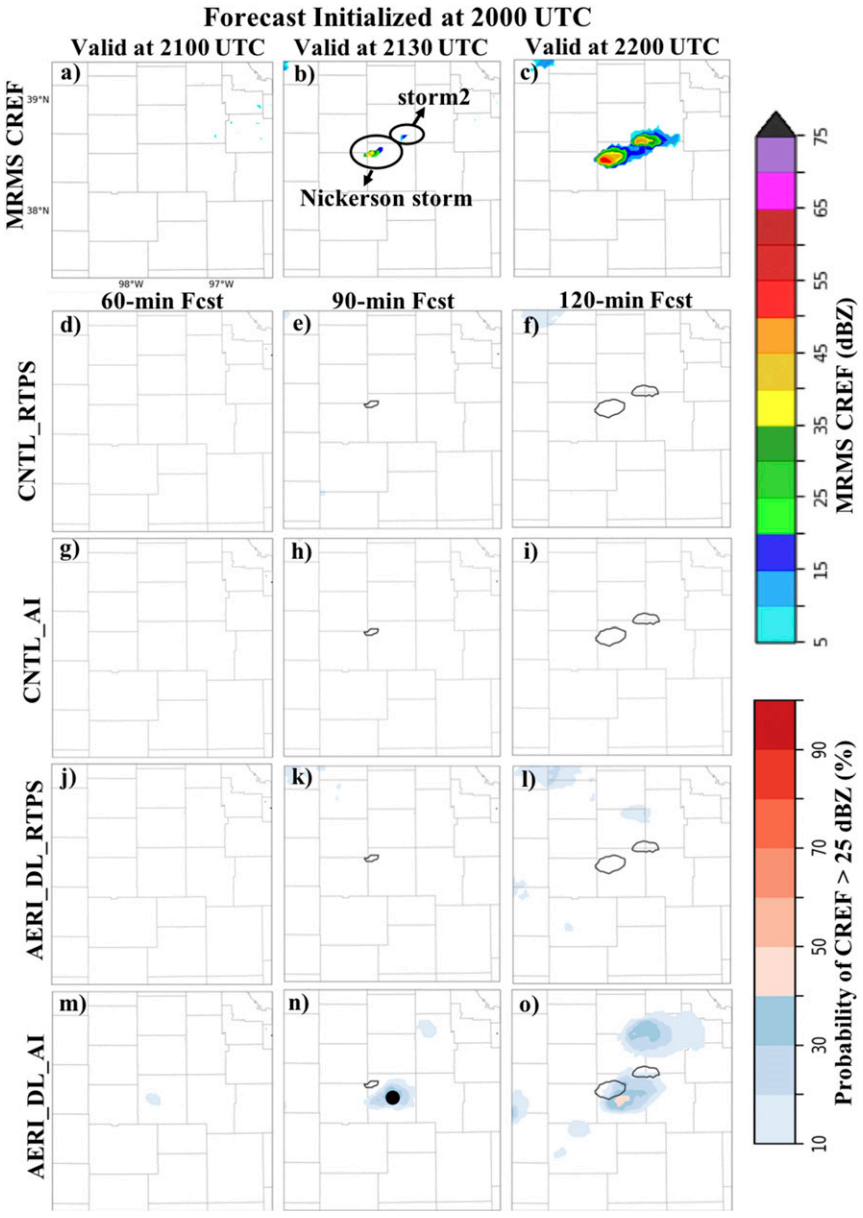

FIG. 5. Observed MRMS CREF at (a) 2100, (b) 2130, and (c) 2200 UTC 13 Jul 2015. Probability of CREF exceeding 25 dBZ from forecasts initialized at 2000 UTC and valid at (d),(g),(j),(m) 2100, (e),(h),(k),(n) 2130, and (f),(i),(l),(o) 2200 UTC from experiments CNTL_RTPS in (d)–(f), CNTL_AI in (g)–(i), AERI_DL_RTPS in (j)–(l), and AERI_DL_AI in (m)–(o). The black contour in (d)–(o) is the 25-dBZ contour from MRMS CREF. The black dot in (n) is the location of the skew T–log$p$ diagram in Fig. 11.

during the next 1-h forecast period (Figs. 7h,i) and by 2200 UTC, AERI_DL_AI forecasts both the Nickerson and storm2 northeast to the Nickerson storm. Likewise, the individual forecasts from ensemble member 1 demonstrate the initiation of the Nickerson storm around 2130 UTC (Fig. 7n) and its intensification 30 min later (Fig. 7o) together with the formation of storm2 in AERI_DL_AI. Conversely, CNTL_AI fails to forecast the storm during the forecast period either in the ensemble mean (Figs. 7d–f) or individual forecasts (Figs. 7j–l).

The fractions skill score (FSS) is computed for CREF greater than 25 dBZ using a neighborhood approach with two neighborhood radius values, 9 and 18 km, respectively. The calculation is made following the method described in Roberts and Lean (2008)

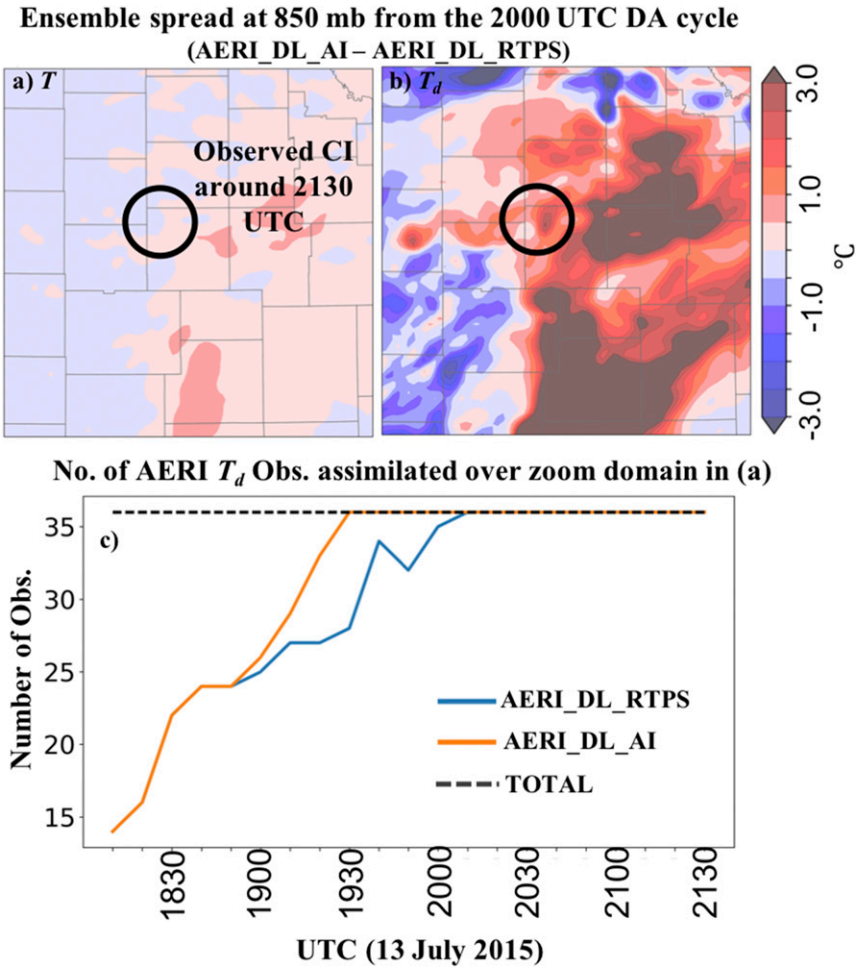

FIG. 6. The differences in the ensemble spread at 850 hPa from the 2000 UTC DA cycle between AERI_DL_AI and AERI_DL_RTPS experiments for (a) T and (b) T_d. The warmer (cooler) color means AI has larger (smaller) spread than RTPS. The black circle overlaid is the observed CI of the Nickerson supercell around 2130 UTC. (c) The number of AERI T_d observations assimilated over the domain in (a) from AERI_DL_AI and AERI_DL_RTPS experiments. The black dashed line is the total number of AERI T_d observations available during DA.

and Schwartz et al. (2010). Not surprisingly, the AERI_DL_AI yields higher FSS compared to CNTL_AI during ~1.5–3 h forecasts (Fig. 8). The higher FSS indicates higher values of probability and smaller location displacement in the AERI_DL_AI. The zero FSS value during the 0–1.25-h period in both experiments is due to the absence of convection during that time period over that area. As expected, the larger neighborhood radius generates higher FSS.

Similar results also are seen from the forecasts initialized at 2100 UTC, which is after six additional DA cycles. The AERI_DL_AI experiment predicts CI for the Nickerson supercell with higher than 30% probability values with a southeastward displacement in location. The CNTL_AI experiment again fails to forecast CI. Neither AERI_DL_AI nor CNTL_AI forecast the CI for the Nickerson supercell at the correct time (not shown) from earlier analyses (before 2000 UTC). Thus, the assimilation of AERI and DL help initiate the Nickerson storm as early as 90 min in advance.

As mentioned in section 2, the Nickerson storm initiated around the intersection of a pressure trough and dryline between 2100 and 2130 UTC as shown in the surface analysis in Figs. 1b and 1d. Compared to CNTL_AI, the AERI_DL_AI experiment forecasts stronger low-level convergence along the pressure trough (Figs. 9a,b) around the CI location. The differences are greater than $30 \times 10^{-5}\,s^{-1}$ (Fig. 9c). The stronger low-level convergence in AERI_DL_AI experiment helps lifting parcels to reach LFC. The low-level moisture near the storm especially from the east and southeast also is enhanced by assimilating AERI

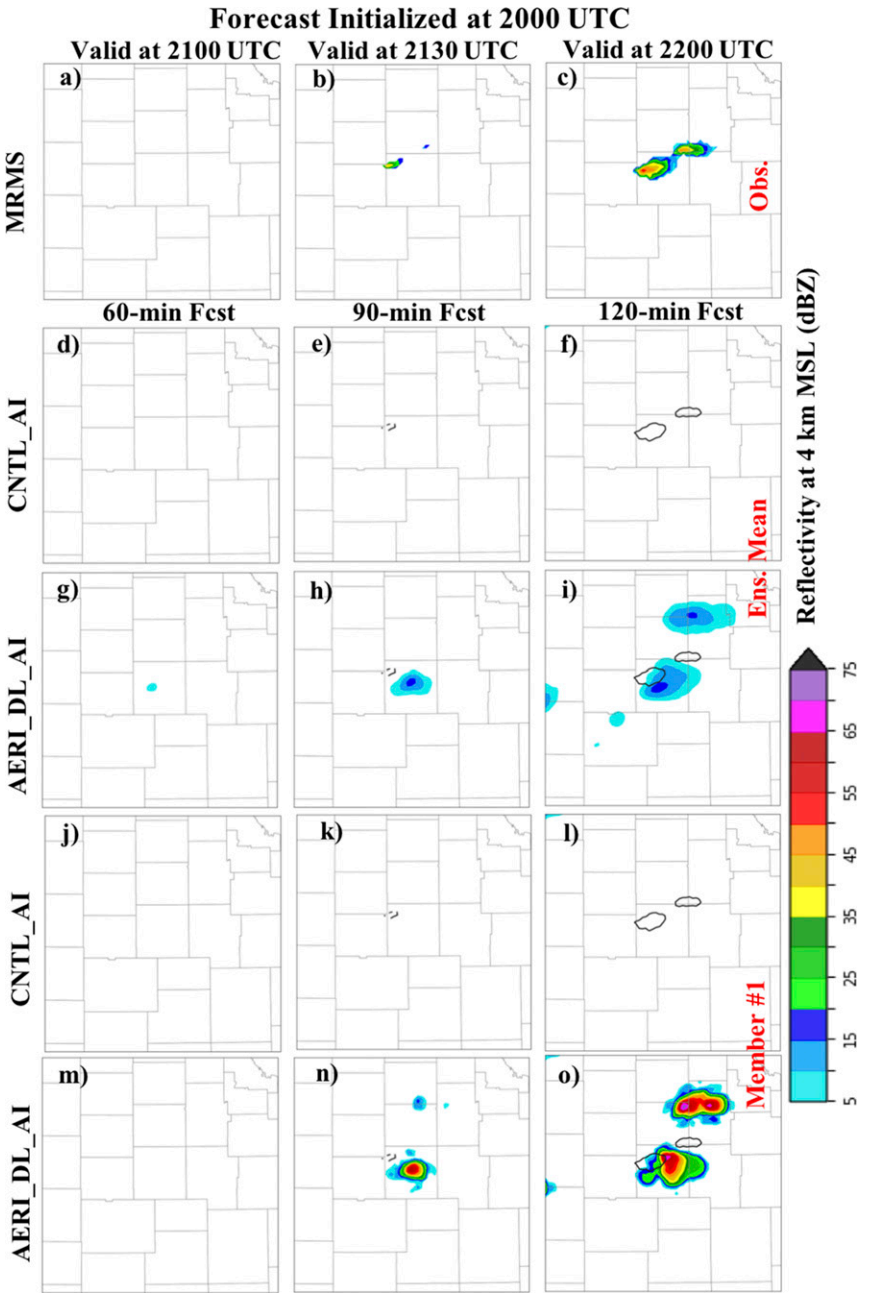

FIG. 7. Observed MRMS reflectivity at 4 km MSL from (a) 2100, (b) 2130, and (c) 2200 UTC 13 Jul 2015. The ensemble mean reflectivity forecasts at 4 km MSL initialized from 2000 UTC analyses and valid at (d),(g) 2100, (e),(h) 2130, and (f),(i) 2200 UTC from experiments CNTL_AI in (d)–(f) and AERI_DL_AI in (g)–(i). The reflectivity forecasts of member 1 at 4 km MSL initialized from 2000 UTC analyses and valid at (j),(m) 2100, (k),(n) 2130, and (l),(o) 2200 UTC from experiments CNTL_AI in (j)–(l) and AERI_DL_AI in (m)–(o). The black contour in (d)–(o) is the 25-dBZ contour from MRMS reflectivity at 4 km MSL.

and DL observations in AERI_DL_AI (Figs. 10a,b). The difference in the moisture between the two experiments is in excess of 3°C (Fig. 10c). The additional moisture in AERI_DL_AI experiment increased the probability of the CI occurrence in the forecast (Crook 1996; Weckwerth 2000). The skew T–log$p$ diagram (Fig. 11) near the CI location (as shown by the black dot in Fig. 5n) from the CNTL_AI and AERI_DL_AI experiments also reveals that the AERI_DL_AI experiment produced higher moisture content at lower levels

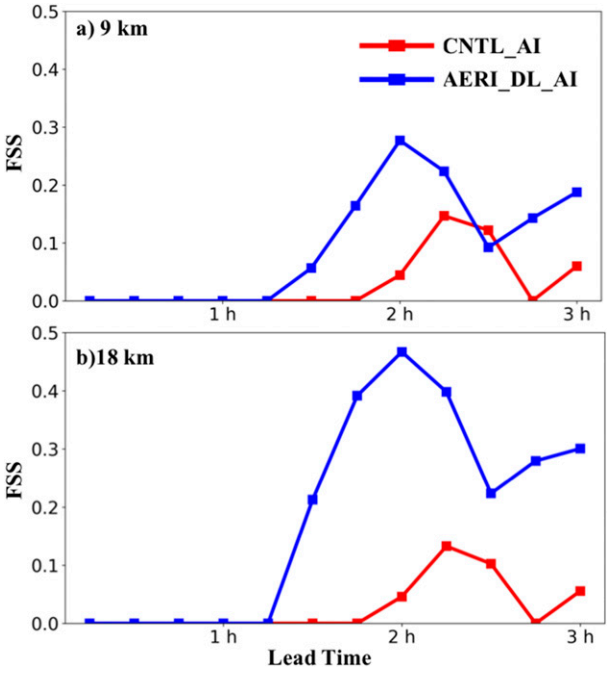

FIG. 8. FSS of forecast CREF greater than 25 dBZ using (a) 9- and (b) 18-km neighborhood radius. The red line indicates CNTL_AI experiment, and the blue line represents AERI_DL_AI experiment. Forecast is initialized at 2000 UTC. The domain used for calculating the FSS is the same as in Fig. 5.

especially between 900 and 700 hPa compared to the CNTL_AI experiment (Figs. 11a,b). Similar results are found in near-storm environment (not shown).

Results discussed above indicate that the assimilation of AERI and DL BL observations increase the moisture in the near-storm environment and low-level convergence along the pressure trough, which likely initiate convection in the forecast. The AERI_DL_AI experiment forecasts CI with 90-min lead time. In contrast, the CNTL_AI experiment fails to forecast CI.

b. *Ensemble forecast after convective initiation*

Another experiment, COMB_AI, is conducted to examine whether the positive impact of assimilating AERI and DL continues after the CI occurrence. The COMB_AI is identical to AERI_DL_AI until 2100 UTC DA cycle (which is approximately 30 min before CI). Starting from 2110 UTC DA cycle, COMB_AI only assimilates observations that are identical to the observations assimilated in CNTL_AI experiment. In short, COMB_AI starts from the AERI_DL_AI analyses at 2100 UTC but withholds AERI and DL observations during the remaining DA cycles. The CNTL_AI analyses fail to initiate convection at 2130 and 2200 UTC (Figs. 12b,f), but AERI_DL_AI analyses produces ~30% Prob_CREF25 for the Nickerson storm with a southeastward displacement at 2130 UTC (Fig. 12c) and the analyses Prob_CREF25 values increase to above 90% after three additional assimilation cycles (Fig. 12g). The analyses from AERI_DL_AI at 2300 UTC and 2330 UTC show Prob_CREF40 values higher than 90% for the Nickerson supercell at approximately the correct location (Figs. 12k,o). The CNTL_AI analyses indicates high Prob_CREF40 values at 2330 UTC, but over a much smaller area (Fig. 12n). Starting from the same background at 2110 UTC, the COMB_AI experiment (Figs. 12d,h,l,p) produces similar probabilities as AERI_DL_AI does (Figs. 12c,g,k,o).

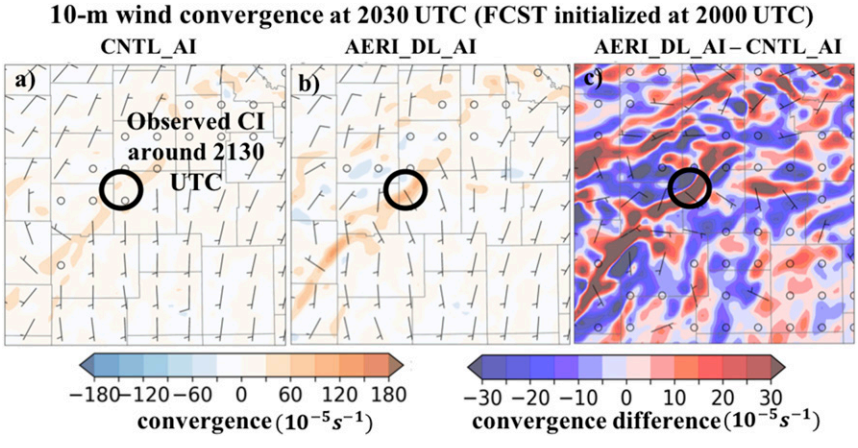

FIG. 9. The 30-min forecast ensemble mean low-level (10 m) wind convergence (10^{-5} s^{-1}) valid at 2030 UTC for (a) the CNTL_AI experiment, (b) the AERI_DL_AI experiment, and (c) the difference between the two experiments (AERI_DL_AI − CNTL_AI). The black circle overlaid is the observed CI of the Nickerson supercell around 2130 UTC.

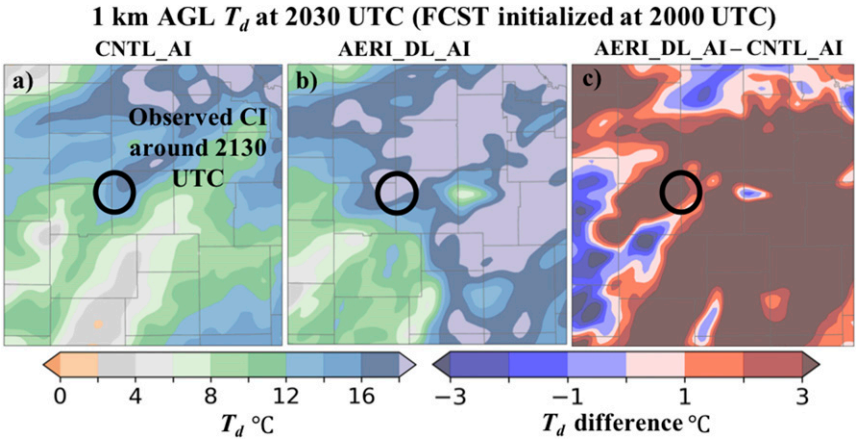

FIG. 10. The 30-min forecast ensemble mean dewpoint temperature at 1 km AGL valid at 2030 UTC for (a) the CNTL_AI experiment, (b) the AERI_DL_AI experiment, and (c) the difference between the two experiments (AERI_DL_AI − CNTL_AI). The black circle overlaid is the observed CI of the Nickerson supercell around 2130 UTC.

Compared to AERI_DL_AI, a significantly smaller number of radar reflectivity observations are assimilated in CNTL_AI after ~2130 UTC, both on the entire convective-scale domain (Fig. 13a) and over a smaller area covering the Nickerson supercell (Fig. 13b). The CNTL_AI experiment fails to initiate CI around ~2130 UTC, rejects most of the radar reflectivity observations in the EnKF outlier check (Fig. 13b), in particular during 2130–2200 UTC time period, and a few reflectivity observations are assimilated during the later DA cycles. On the other hand, more than 30% of the ensemble members in AERI_DL_AI and COMB_AI predict CI around 2130 UTC. As a result, a relatively larger number of reflectivity observations from the incipient Nickerson cell during ~2145–2200 UTC time period pass the

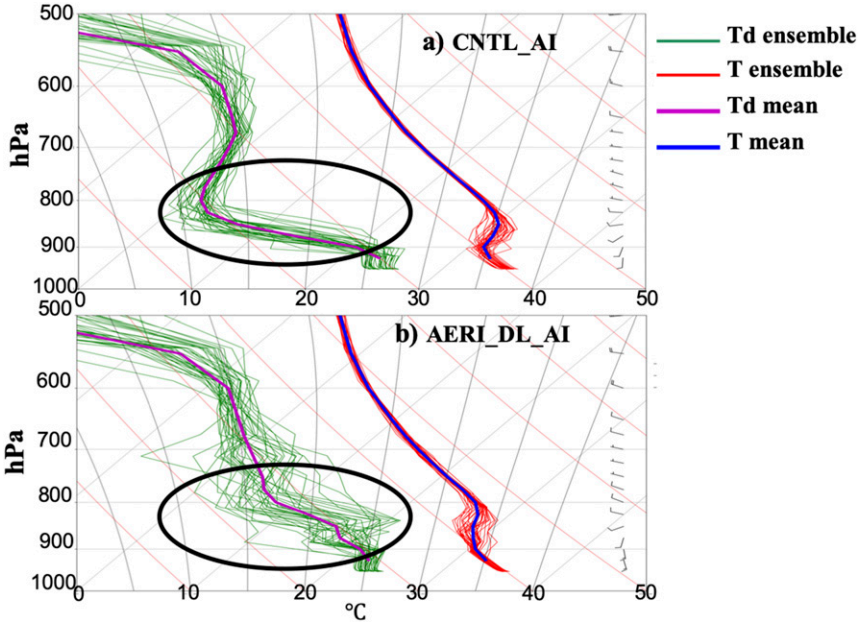

FIG. 11. Skew T–log$p$ diagram from the 30-min forecast valid at 2030 UTC from (a) CNTL_AI and (b) AERI_DL_AI experiments at the location shown by the black dot in Fig. 5n. The thin green lines are the dewpoint temperature from the ensemble members, and the purple line is the ensemble mean; the thin red lines indicate the temperature from the ensemble members, and the blue line indicates the ensemble mean.

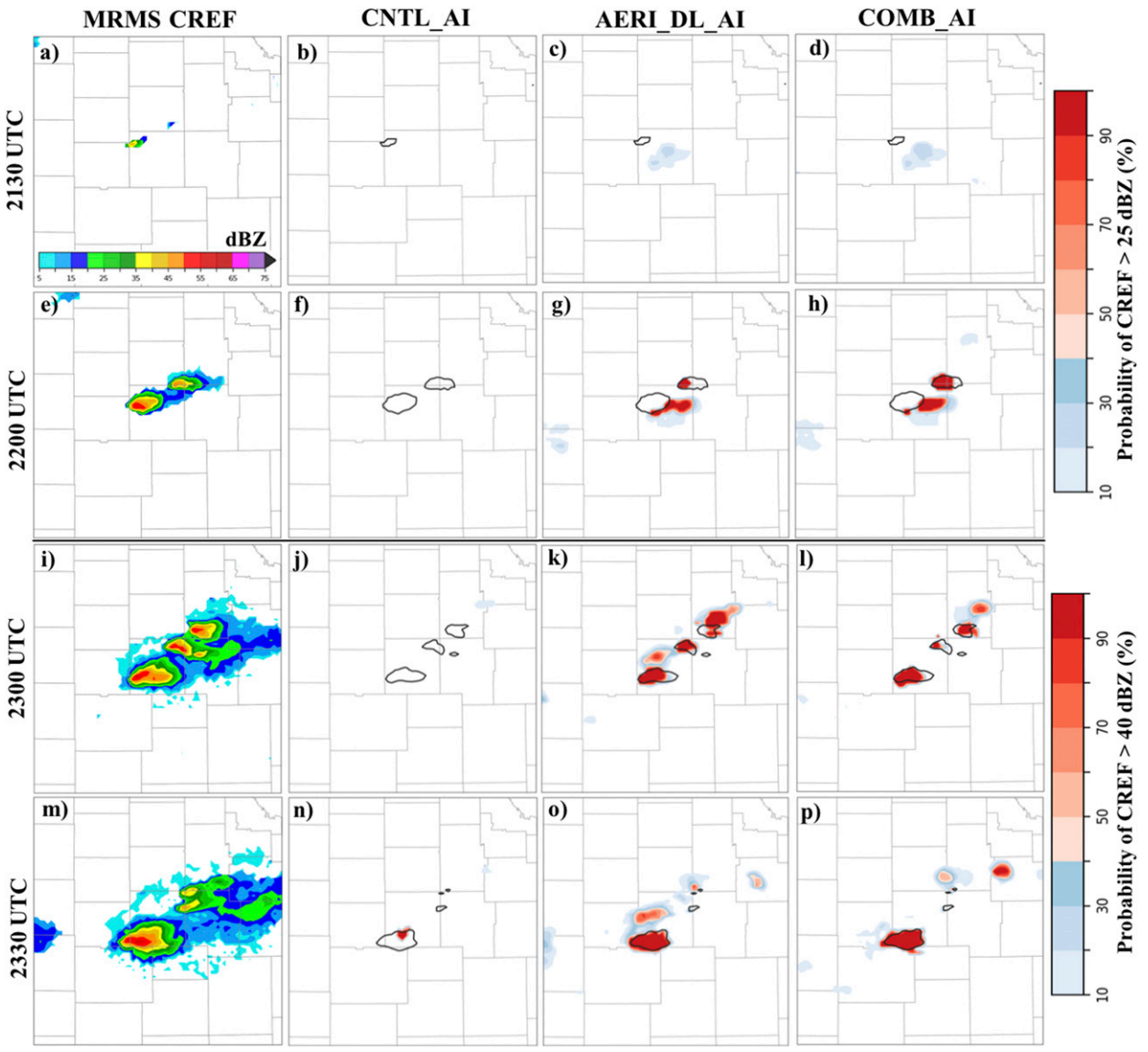

FIG. 12. (first column) The observed MRMS CREF and the Prob_CREF25 from the analyses valid at (a)–(d) 2130 and (e)–(h) 2200 UTC, and the Prob_CREF40 from the analyses valid at (i)–(l) 2300 and (m)–(p) 2330 UTC from the (second column) CNTL_AI, (third column) AERI_DL_AI, and (fourth column) COMB_AI experiments. The black contour in (b)–(d), (f)–(h), (j)–(l), and (n)–(p) is the 40-dBZ contour from MRMS CREF.

outlier check and are assimilated in AERI_DL_AI and COMB_AI experiments (Fig. 13b). Not surprisingly, the number of radar reflectivity observations assimilated in COMB_AI is close to that in AERI_DL_AI (Figs. 13a,b), which explains the overall similar behavior of COMB_AI and AERI_DL_AI (Figs. 12d,h,l,p with Figs. 12c,g,k,o) The similar number of reflectivity observations assimilated in all three experiments during the early DA period (1810–2130 UTC; Fig. 13a) are mainly from the convection over the northern part of domain (Figs. 1c–e).

The 30-, 60-, 90- and 120-min forecasts (Figs. 14i–l) initialized from the 2300 UTC analyses (Fig. 12k) generate higher Prob_CREF40 values near the Nickerson storm in the AERI_DL_AI experiment with a systematic displacement error. In contrast, the CNTL_AI forecasts low Prob_CREF40 (Fig. 14e) values 30-min into the forecast and then the probability values disappear (Fig. 14f). COMB_AI produces higher Prob_CREF40 (Figs. 14m–p) compared to that from the CNTL_AI (Figs. 14e–h) indicating the positive impact of assimilating AERI and DL during the early assimilation cycle. However, the

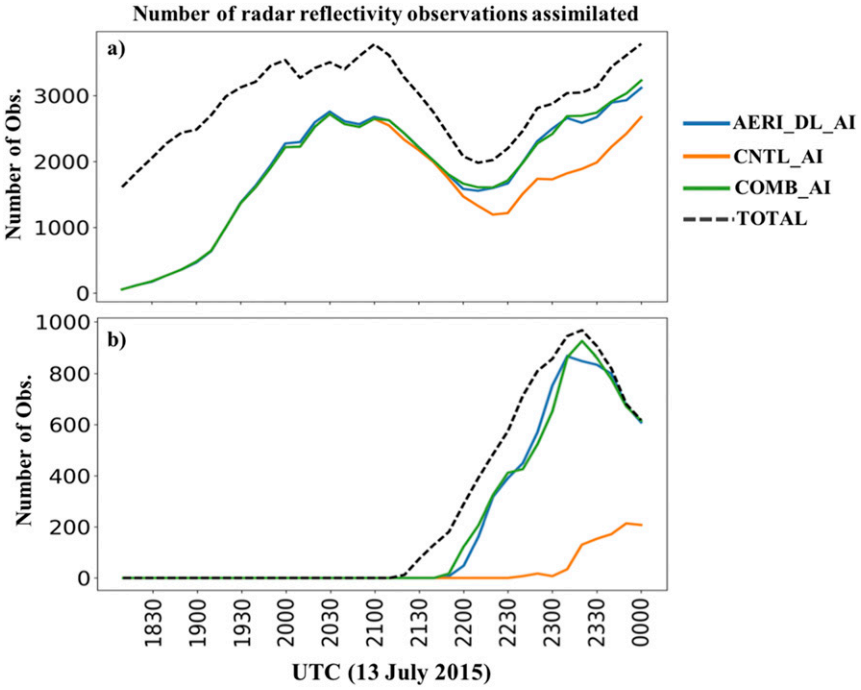

FIG. 13. The total number of available radar reflectivity observations (only the nonzero values; dashed black line) and the number of reflectivity assimilated in the CNTL_AI (orange line), AERI_DL_AI (blue line), and COMB_AI (green line) experiments after passing the EnKF outlier check over the (a) entire convective-scale domain as in Fig. 4b and (b) over a smaller domain centered on Nickerson supercell area as in Fig. 5a.

high Prob_CREF40 values from AERI_DL_AI (Figs. 14i–l) compared to that from COMB_AI (Figs. 14m–p) clearly indicates the benefit of assimilating AERI and DL in forecasting the evolution of the storm after initiation.

c. *The AERI_AI and DL_AI experiments*

As mentioned earlier, the AERI_AI and DL_AI experiments are designed to examine which of the two observing platforms has more impact on the ensemble forecasts. The 90-min forecast initialized from the 2000 UTC analysis generates ~10% Prob_CREF25 near the Nickerson storm for the AERI_AI experiment (Fig. 15e), and the forecast probability increases to as high as 40% (Fig. 15f) 2 h into the forecast. Similar to AERI_DL_AI experiment (Figs. 5m–o), a southeastward displacement is noticed in the CI location for the Nickerson storm but a northward displacement for storm2 (Figs. 15e–f). In contrast, DL_AI (Figs. 15g–i) and CNTL_AI (Figs. 15a–c) fail to initiate the storm during the forecast period. Compared to CNTL_AI analyses at 2300 UTC, which fail to generate any Prob_CREF40 values for the Nickerson storm (Fig. 16a), DL_AI experiment generates high Prob_CREF40 value but over a very small area (Fig. 16g). In contrast, the AERI_AI experiment generates high Prob_CREF40 with larger areal coverage over the observed Nickerson tornadic supercell storm (Fig. 16d) in the analyses. The forecast storm from AERI_AI slowly weakens during the next 30-min forecast period (Figs. 16e–f).

The overall results from Figs. 15 and 16 indicate that the AERI thermodynamic retrievals have a larger impact on the ensemble analyses and short-term forecast of the Nickerson supercell storm, compared to the kinematic retrievals from DL. The CI forecast initialized at 2000 UTC from AERI_DL_AI (Figs. 5m–o) has higher Prob_CREF25 values for the Nickerson storm compared to that from either AERI_AI or DL_AI (Fig. 15) experiment. The evolution of the storm after CI in AERI_DL_AI (Figs. 14i–l) compared to that from AERI_AI and DL_AI (Fig. 16) also suggests positive impact when retrievals from both instruments are assimilated together.

6. Summary and conclusions

This study examines the impact of assimilating BL profiles from two ground-based remote sensing instruments, namely the AERI and DL, on the ensemble

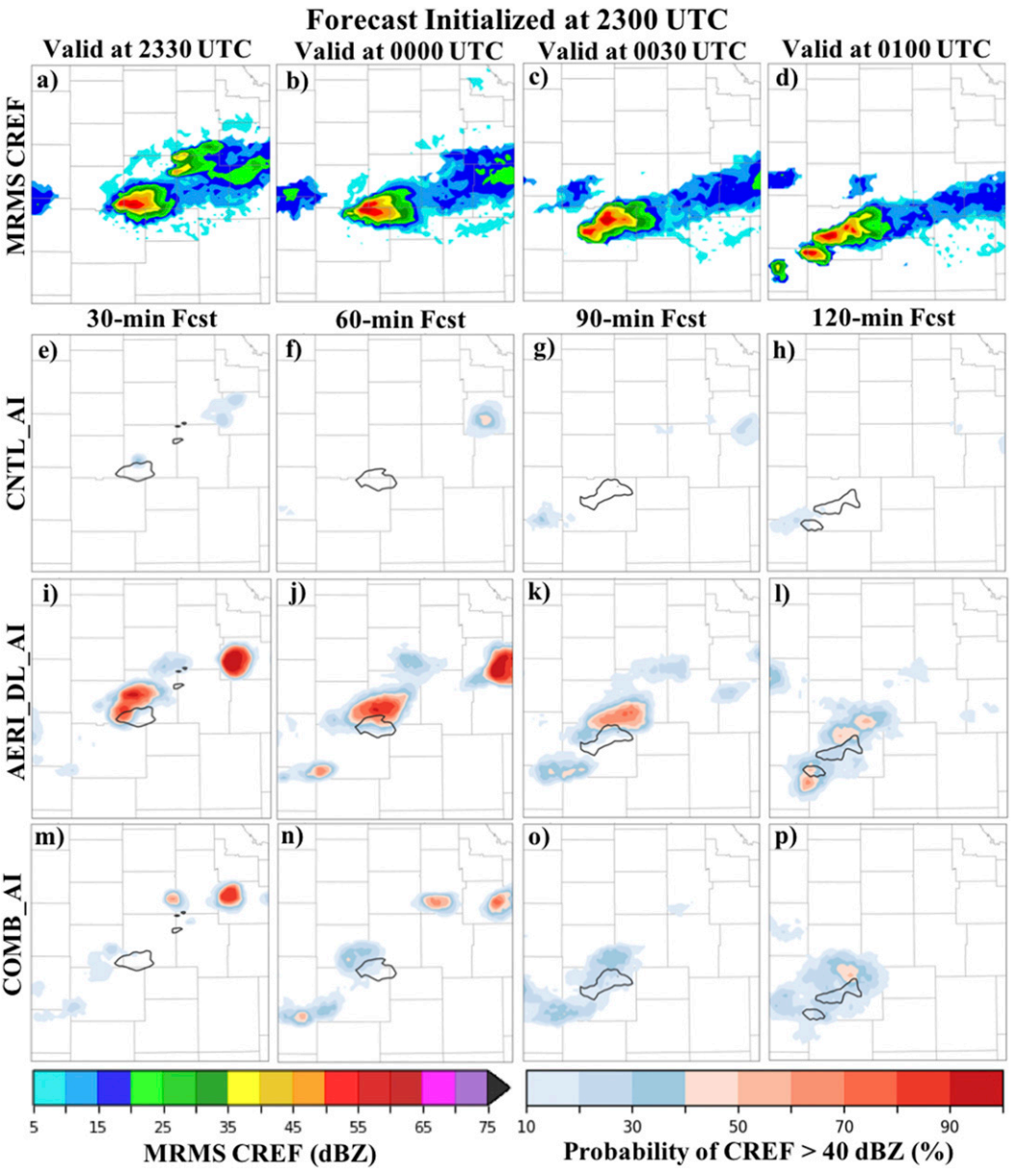

FIG. 14. (first row) The observed MRMS CREF and forecast Prob_CREF40 initialized at 2300 UTC and valid at (e),(i),(m) 2330, (f),(j),(n) 0000, (g),(k),(o) 0030, and (h),(l),(p) 0100 UTC from the (second row) CNTL_AI, (third row) AERI_DL_AI, and (fourth row) COMB_AI experiments. The black contour in (e)–(p) is the 40-dBZ contour from MRMS CREF.

analyses and forecasts of a tornadic supercell event on 13 July 2015 in Kansas. The observations include temperature and moisture profiles from the AERI and horizontal wind profiles from the DL. The goal is to evaluate if assimilating these additional high temporal resolution near-storm BL profiles helps improve the ensemble forecasts of CI and subsequent evolution of the tornadic supercell.

Six sets of convective-scale ensemble DA and prediction experiments are conducted using the WRF-ARW Model and GSI-EnKF DA system. Both the control and AERI_DL experiments use the same initial and boundary conditions. The control experiments (CNTL_AI and CNTL_RTPS) assimilate NWS routinely available conventional, Oklahoma mesonet as well as WSR-88D radar reflectivity and radial velocity observations, and the AERI_DL experiments (AERI_DL_AI and AERI_DL_RTPS) assimilate AERI and DL profile retrievals in addition to all other observations assimilated in the control experiment. The impact of the choice of the inflation method in

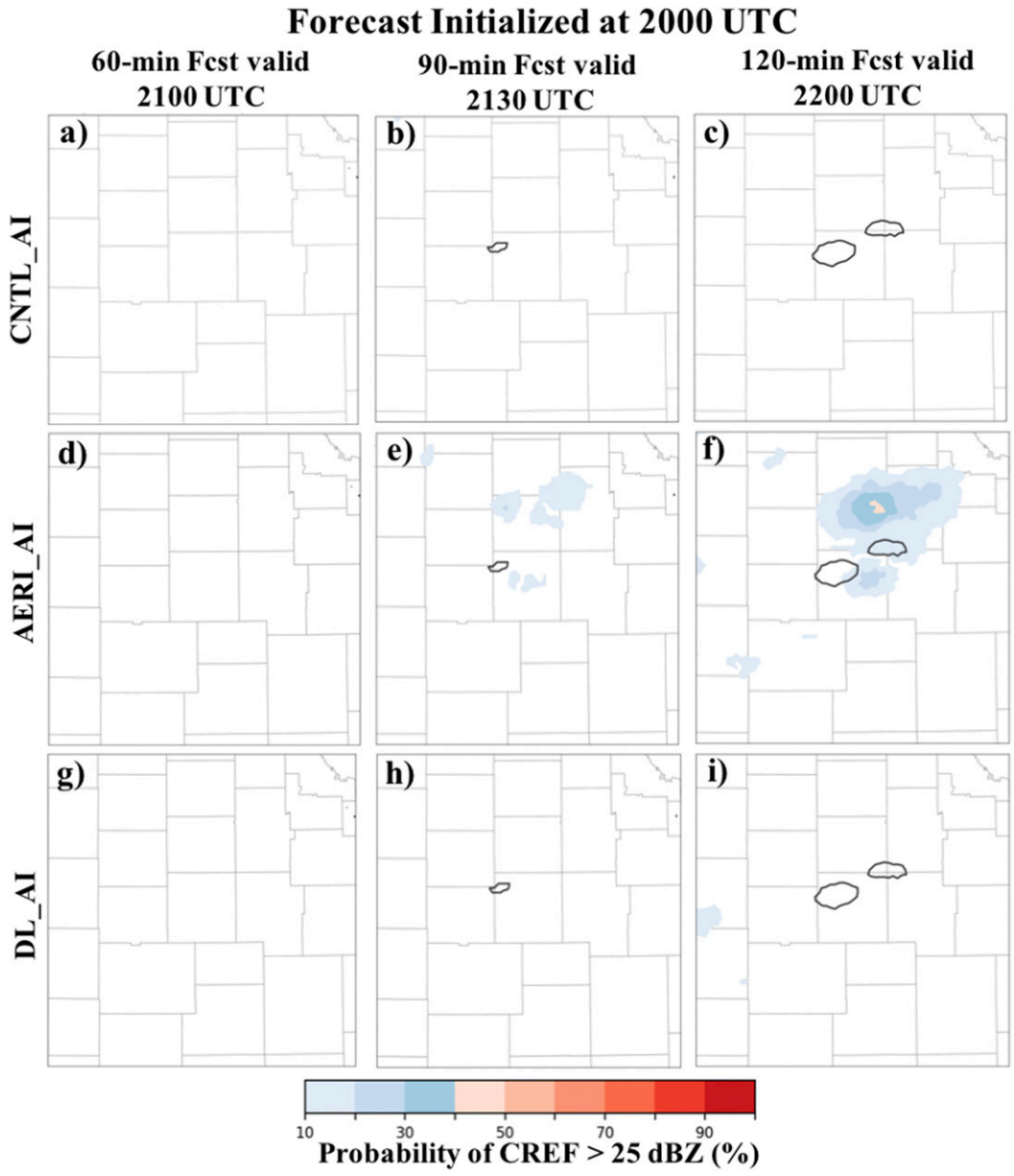

FIG. 15. The Prob_CREF25 from forecasts initialized at 2000 UTC and valid at (a),(d),(g) 2100, (b),(e),(h) 2130, and (c),(f),(i) 2200 UTC from the (top) CNTL_AI, (middle) AERI_AI, and (bottom) DL_AI experiments. The thick black contour overlaid is the 25-dB*Z* MRMS CREF.

convective-scale ensemble DA and prediction is evaluated by evaluating two commonly used inflation technique, the RTPS and AI technique. To examine which instrument has a larger impact, two additional experiments are performed, namely AERI_AI that withholds DL observations and DL_AI that withholds AERI retrievals from AERI_DL_AI experiment.

Results suggest that the forecast is sensitive to the choice of the inflation technique utilized in the convective-scale cycled DA. The assimilation of AERI and DL retrievals using the spatially and temporally varying AI technique forecasts the CI with a 90-min lead time, whereas the same experiment using the RTPS method fails to initiate CI. Cycled AI created favorable spread in the ensemble that facilitated the assimilation of a larger number of AERI and DL observations than RTPS. Assimilating the high temporal resolution thermodynamic and kinematic profiler observations from AERI and DL improve CI forecasts both in terms of timing and location.

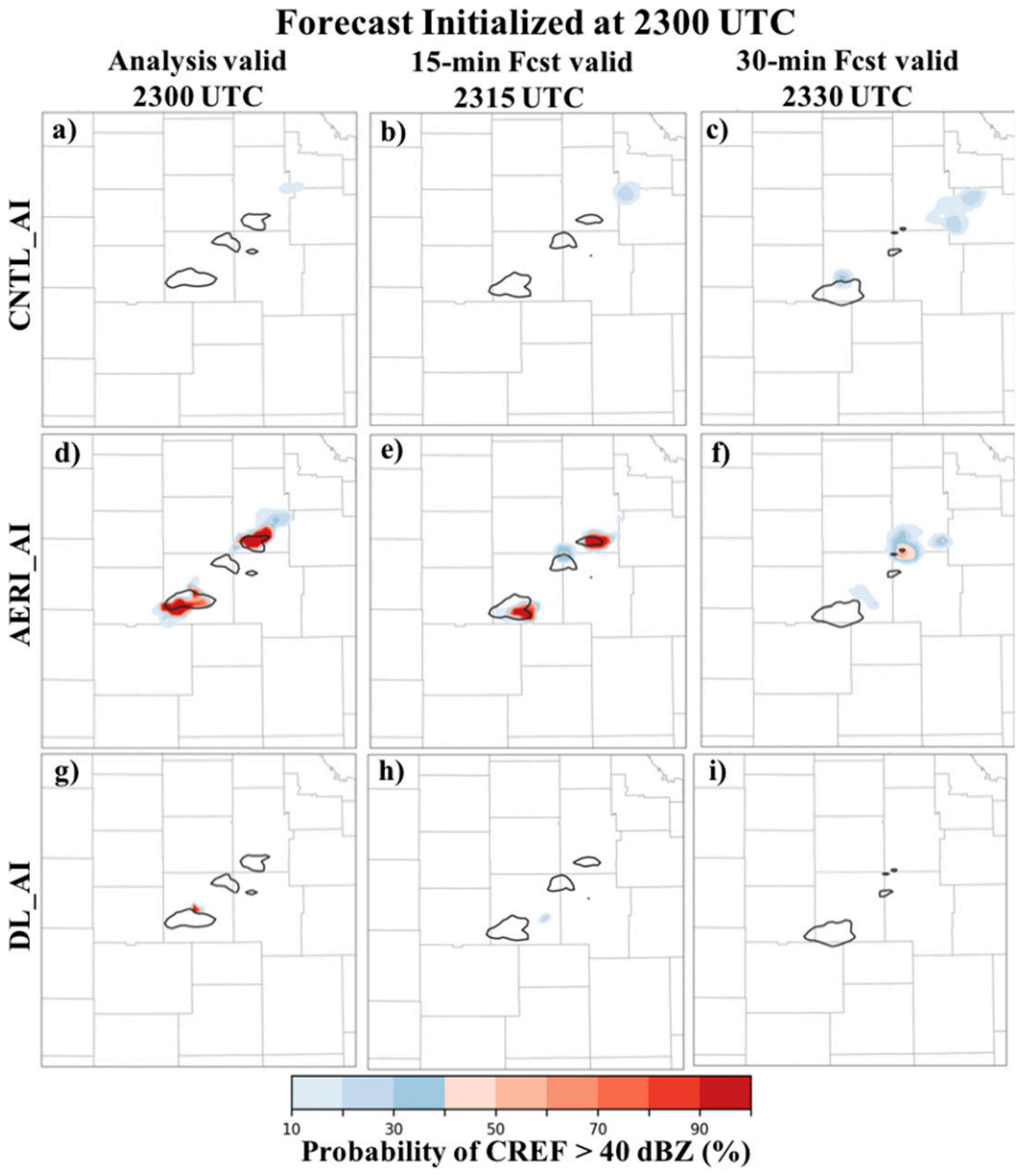

FIG. 16. The Prob_CREF40 from analysis at (left) 2300 UTC, (center) 15-min forecast valid at 2315 UTC, and (right) 30-min forecast valid at 2330 UTC for the (a)–(c) CNTL_AI, (d)–(f) AERI_AI, and (g)–(i) DL_AI experiments. The thick black contour overlaid is the 40-dB*Z* MRMS CREF.

Detailed analysis indicates that the AERI and DL observations create a more favorable BL environment for CI. The additional moisture in the near-storm environment and stronger low-level convergence along the pressure trough in AERI_DL_AI experiment contributes to the initiation of the Nickerson tornadic supercell. Results also suggest that the CI prediction in AERI_DL_AI experiment enables a larger number of radar reflectivity observations to pass the EnKF outlier check compared to that from CNTL_AI experiment, resulting in an improved ensemble initial condition and forecast. The improvements in the forecast of the supercell storm is more pronounced during the first 3 h of the forecast period. Comparison between AERI_AI and DL_AI experiments indicates that the moisture from the AERI likely has a larger impact on CI and early evolution of the storm than that from DL winds. Assimilating both AERI and DL retrievals improves the storm environment, which results in an improved forecast, whereas, withholding either DL or AERI

from the AERI_DL_AI experiment degrades the forecast.

This study shows the potential of assimilating AERI and DL observations into NWP to improve short-term forecasts of CI and the subsequent evolution for a supercell tornado event. A network of these types of BL profiling instruments over the CONUS may benefit a wide range of applications, in particular the short-term prediction of hazardous convective weather by providing better NWP initial conditions. This study also reveals that convective-scale DA system is sensitive to the choice of the inflation technique utilized in the configuration. However, the results from this single case study should be interpreted cautiously. Coniglio et al. (2019) have shown the positive impact of assimilating AERI and DL profiles on the early evolution of thunderstorms using several severe weather days. However, they only used observations from one station. More studies need to be performed over multiple cases to assess the robustness of the impact of assimilating a network of BL instruments and the AI technique in convective-scale ensemble DA and prediction system.

Acknowledgments. This work supported by a grant from the FY2016 Joint Technology Transfer Initiative Program within NOAA/OAR Office of Weather and Air Quality under Grant NA16OAR4590242. Additional support is provided by NOAA/Office of Oceanic and Atmospheric Research under NOAA–University of Oklahoma Cooperative Agreement NA11OAR4320072, U.S. Department of Commerce. The last author is also supported by AGS-1359703. The authors thank Craig Schwartz and two anonymous reviewers for the constructive review. The authors also want to thank Jidong Gao for internal review, and Derek Stratman and Greg Blumberg for their helpful suggestions over the course of the research. IT support was provided by Gerry Creager, Robert Coggins, Brett Morrow, and Steve Fletcher.

REFERENCES

Anderson, J. L., 2009: Spatially and temporally varying adaptive covariance inflation for ensemble filters. *Tellus*, **61A**, 72–83, https://doi.org/10.1111/j.1600-0870.2008.00361.x.

——, and N. Collins, 2007: Scalable implementations of ensemble filter algorithms for data assimilation. *J. Atmos. Oceanic Technol.*, **24**, 1452–1463, https://doi.org/10.1175/JTECH2049.1.

Berger, H., and M. Forsythe, 2004: Satellite wind superobbing. Met Office Forecasting Research Tech. Rep. 451, 33 pp.

Blumberg, W., D. Turner, U. Löhnert, and S. Castleberry, 2015: Ground-based temperature and humidity profiling using spectral infrared and microwave observations. Part II: Actual retrieval performance in clear-sky and cloudy conditions. *J. Appl. Meteor. Climatol.*, **54**, 2305–2319, https://doi.org/10.1175/JAMC-D-15-0005.1.

Chai, T., C.-L. Lin, and R. K. Newsom, 2004: Retrieval of microscale flow structures from high-resolution Doppler lidar data using an adjoint model. *J. Atmos. Sci.*, **61**, 1500–1520, https://doi.org/10.1175/1520-0469(2004)061<1500:ROMFSF>2.0.CO;2.

Coniglio, M. C., J. Correia Jr., P. T. Marsh, and F. Kong, 2013: Verification of convection-allowing WRF model forecasts of the planetary boundary layer using sounding observations. *Wea. Forecasting*, **28**, 842–862, https://doi.org/10.1175/WAF-D-12-00103.1.

——, S. M. Hitchcock, and K. H. Knopfmeier, 2016: Impact of assimilating preconvective upsonde observations on short-term forecasts of convection observed during MPEX. *Mon. Wea. Rev.*, **144**, 4301–4325, https://doi.org/10.1175/MWR-D-16-0091.1.

——, G. S. Romine, D. D. Turner, and R. D. Torn, 2019: Impacts of targeted AERI and Doppler lidar wind retrievals on short-term forecasts of the initiation and early evolution of thunderstorms. *Mon. Wea. Rev.*, **147**, 1149–1170, https://doi.org/10.1175/MWR-D-18-0351.1.

Crook, N. A., 1996: Sensitivity of moist convection forced by boundary layer processes to low-level thermodynamic fields. *Mon. Wea. Rev.*, **124**, 1767–1785, https://doi.org/10.1175/1520-0493(1996)124<1767:SOMCFB>2.0.CO;2.

Degelia, S., X. Wang, D. Stensrud, and A. Johnson, 2018: Understanding the impact of radar and in situ observations on the prediction of a nocturnal convection initiation event on 25 June 2013 using an ensemble-based multiscale data assimilation system. *Mon. Wea. Rev.*, **146**, 1837–1859, https://doi.org/10.1175/MWR-D-17-0128.1.

Dowell, D. C., and L. J. Wicker, 2009: Additive noise for storm-scale ensemble data assimilation. *J. Atmos. Oceanic Technol.*, **26**, 911–927, https://doi.org/10.1175/2008JTECHA1156.1.

——, F. Zhang, L. J. Wicker, C. Snyder, and N. A. Crook, 2004: Wind and temperature retrievals in the 17 May 1981 Arcadia, Oklahoma, supercell: Ensemble Kalman filter experiments. *Mon. Wea. Rev.*, **132**, 1982–2005, https://doi.org/10.1175/1520-0493(2004)132<1982:WATRIT>2.0.CO;2.

Feltz, W. F., and J. R. Mecikalski, 2002: Monitoring high-temporal-resolution convective stability indices using the ground-based Atmospheric Emitted Radiance Interferometer (AERI) during the 3 May 1999 Oklahoma–Kansas tornado outbreak. *Wea. Forecasting*, **17**, 445–455, https://doi.org/10.1175/1520-0434(2002)017<0445:MHTRCS>2.0.CO;2.

——, W. L. Smith, R. O. Knuteson, H. E. Revercomb, H. M. Woolf, and H. B. Howell, 1998: Meteorological applications of temperature and water vapor retrievals from the ground-based Atmospheric Emitted Radiance Interferometer (AERI). *J. Appl. Meteor.*, **37**, 857–875, https://doi.org/10.1175/1520-0450(1998)037<0857:MAOTAW>2.0.CO;2.

Fujita, T., D. J. Stensrud, and D. C. Dowell, 2007: Surface data assimilation using an ensemble Kalman filter approach with initial condition and model physics uncertainties. *Mon. Wea. Rev.*, **135**, 1846–1868, https://doi.org/10.1175/MWR3391.1.

Gao, J., and D. J. Stensrud, 2012: Assimilation of reflectivity data in a convective-scale, cycled 3DVAR framework with hydrometeor classification. *J. Atmos. Sci.*, **69**, 1054–1065, https://doi.org/10.1175/JAS-D-11-0162.1.

Gaspari, G., and S. E. Cohn, 1999: Construction of correlation functions in two and three dimensions. *Quart. J. Roy. Meteor. Soc.*, **125**, 723–757, https://doi.org/10.1002/qj.49712555417.

Geer, A. J., and P. Bauer, 2011: Observation errors in all-sky data assimilation. *Quart. J. Roy. Meteor. Soc.*, **137**, 2024–2037, https://doi.org/10.1002/qj.830.

Geerts, B., and Coauthors, 2017: The 2015 Plains Elevated Convection At Night field project. *Bull. Amer. Meteor. Soc.*, **98**, 767–786, https://doi.org/10.1175/BAMS-D-15-00257.1.

Ha, S.-Y., and C. Snyder, 2014: Influence of surface observations in mesoscale data assimilation using an ensemble Kalman filter. *Mon. Wea. Rev.*, **142**, 1489–1508, https://doi.org/10.1175/MWR-D-13-00108.1.

Hitchcock, S. M., M. C. Coniglio, and K. H. Knopfmeier, 2016: Impact of MPEX upsonde observations on ensemble analyses and forecasts of the 31 May 2013 convective event over Oklahoma. *Mon. Wea. Rev.*, **144**, 2889–2913, https://doi.org/10.1175/MWR-D-15-0344.1.

Hodyss, D., W. F. Campbell, and J. S. Whitaker, 2016: Observation-dependent posterior inflation for the ensemble Kalman filter. *Mon. Wea. Rev.*, **144**, 2667–2684, https://doi.org/10.1175/MWR-D-15-0329.1.

Hoff, R. M., and R. M. Hardesty, Eds., 2012: Thermodynamic Profiling Technologies Workshop Report to the National Science Foundation and the National Weather Service. NCAR Tech. Note NCAR/TN-4881STR, 80 pp.

Houtekamer, P., and F. Zhang, 2016: Review of the ensemble Kalman filter for atmospheric data assimilation. *Mon. Wea. Rev.*, **144**, 4489–4532, https://doi.org/10.1175/MWR-D-15-0440.1.

Hu, M., S. G. Benjamin, T. T. Ladwig, D. C. Dowell, S. S. Weygandt, C. R. Alexander, and J. S. Whitaker, 2017a: GSI three-dimensional ensemble–variational hybrid data assimilation using a global ensemble for the regional Rapid Refresh model. *Mon. Wea. Rev.*, **145**, 4205–4225, https://doi.org/10.1175/MWR-D-16-0418.1.

——, G. Ge, H. Shao, D. Stark, K. Newman, C. Zhou, J. Beck, and X. Zhang, 2017b: Gridpoint Statistical Interpolation user's guide version 3.6. Developmental Testbed Center, 158 pp., https://dtcenter.org/com-GSI/users/docs/users_guide/GSIUserGuide_v3.6.pdf.

Johnson, A., X. Wang, J. R. Carley, L. J. Wicker, and C. Karstens, 2015: A comparison of multiscale GSI-based EnKF and 3DVar data assimilation using radar and conventional observations for midlatitude convective-scale precipitation forecasts. *Mon. Wea. Rev.*, **143**, 3087–3108, https://doi.org/10.1175/MWR-D-14-00345.1.

——, ——, K. R. Haghi, and D. B. Parsons, 2018: Evaluation of forecasts of a convectively generated bore using an intensively observed case study from PECAN. *Mon. Wea. Rev.*, **146**, 3097–3122, https://doi.org/10.1175/MWR-D-18-0059.1.

Jones, T. A., and D. J. Stensrud, 2012: Assimilating AIRS temperature and mixing ratio profiles using an ensemble Kalman filter approach for convective-scale forecasts. *Wea. Forecasting*, **27**, 541–564, https://doi.org/10.1175/WAF-D-11-00090.1.

——, K. Knopfmeier, D. Wheatley, G. Creager, P. Minnis, and R. Palikonda, 2016: Storm-scale data assimilation and ensemble forecasting with the NSSL experimental Warn-on-Forecast system. Part II: Combined radar and satellite data experiments. *Wea. Forecasting*, **31**, 297–327, https://doi.org/10.1175/WAF-D-15-0107.1.

——, X. Wang, P. Skinner, A. Johnson, and Y. Wang, 2018: Assimilation of GOES-13 imager clear-sky water vapor (6.5 μm) radiances into a Warn-on-Forecast system. *Mon. Wea. Rev.*, **146**, 1077–1107, https://doi.org/10.1175/MWR-D-17-0280.1.

Kain, J. S., and Coauthors, 2013: A feasibility study for probabilistic convection initiation forecasts based on explicit numerical guidance. *Bull. Amer. Meteor. Soc.*, **94**, 1213–1225, https://doi.org/10.1175/BAMS-D-11-00264.1.

Klein, P., and Coauthors, 2015: LABLE: A multi-institutional, student-led, atmospheric boundary layer experiment. *Bull. Amer. Meteor. Soc.*, **96**, 1743–1764, https://doi.org/10.1175/BAMS-D-13-00267.1.

Kleist, D. T., D. F. Parrish, J. C. Derber, R. Treadon, W.-S. Wu, and S. Lord, 2009: Introduction of the GSI into the NCEP Global Data Assimilation System. *Wea. Forecasting*, **24**, 1691–1705, https://doi.org/10.1175/2009WAF2222201.1.

Knopfmeier, K. H., and D. J. Stensrud, 2013: Influence of mesonet observations on the accuracy of surface analyses generated by an ensemble Kalman filter. *Wea. Forecasting*, **28**, 815–841, https://doi.org/10.1175/WAF-D-12-00078.1.

Lin, X., and K. G. Hubbard, 2004: Uncertainties of derived dewpoint temperature and relative humidity. *J. Appl. Meteor.*, **43**, 821–825, https://doi.org/10.1175/2100.1.

Liu, H., M. Hu, H. Shao, D. Stark, G. Ge, K. Newman, and J. Whittaker, 2017: Ensemble Kalman Filter (EnKF) user's guide version 1.2. Developmental Testbed Center, 86 pp., https://dtcenter.org/EnKF/users/docs/enkf_users_guide/EnKF_UserGuide_v1.2.pdf.

Lu, X., X. Wang, Y. Li, M. Tong, and X. Ma, 2017a: GSI-based ensemble-variational hybrid data assimilation for HWRF for hurricane initialization and prediction: Impact of various error covariances for airborne radar observation assimilation. *Quart. J. Roy. Meteor. Soc.*, **143**, 223–239, https://doi.org/10.1002/qj.2914.

——, ——, M. Tong, and V. Tallapragada, 2017b: GSI-based, fully cycled, dual resolution hybrid ensemble–variational data assimilation system for HWRF: System description and experiment with Edouard (2014). *Mon. Wea. Rev.*, **145**, 4877–4898, https://doi.org/10.1175/MWR-D-17-0068.1.

National Research Council, 2009: *Observing Weather and Climate from the Ground Up: A Nationwide Network of Networks*. National Academies Press, 250 pp, https://doi.org/10.17226/12540.

——, 2010: *When Weather Matters: Science and Services to Meet Critical Societal Needs*. National Academies Press, 198 pp, https://doi.org/10.17226/12888.

Newsom, R. K., and R. M. Banta, 2004a: Assimilating coherent Doppler lidar measurements into a model of the atmospheric boundary layer. Part I: Algorithm development and sensitivity to measurement error. *J. Atmos. Oceanic Technol.*, **21**, 1328–1345, https://doi.org/10.1175/1520-0426(2004)021<1328:ACDLMI>2.0.CO;2.

——, and ——, 2004b: Assimilating coherent Doppler lidar measurements into a model of the atmospheric boundary layer. Part II: Sensitivity analyses. *J. Atmos. Oceanic Technol.*, **21**, 1809–1824, https://doi.org/10.1175/JTECH-1676.1.

——, D. Ligon, R. Calhoun, R. Heap, E. Cregan, and M. Princevac, 2005: Retrieval of microscale wind and temperature fields from single-and dual-Doppler lidar data. *J. Appl. Meteor.*, **44**, 1324–1345, https://doi.org/10.1175/JAM2280.1.

——, W. A. Brewer, J. M. Wilczak, D. E. Wolfe, S. P. Oncley, and J. K. Lundquist, 2017: Validating precision estimates in horizontal wind measurements from a Doppler lidar. *Atmos. Meas. Tech.*, **10**, 1229, https://doi.org/10.5194/amt-10-1229-2017.

Ochotta, T., C. Gebhardt, D. Saupe, and W. Wergen, 2005: Adaptive thinning of atmospheric observations in data assimilation with vector quantization and filtering methods.

Quart. J. Roy. Meteor. Soc., **131**, 3427–3437, https://doi.org/10.1256/qj.05.94.

Pagowski, M., and G. A. Grell, 2012: Experiments with the assimilation of fine aerosols using an ensemble Kalman filter. *J. Geophys. Res.*, **117**, D21302, https://doi.org/10.1029/2012JD018333.

Pearson, G., F. Davies, and C. Collier, 2009: An analysis of the performance of the UFAM pulsed Doppler lidar for observing the boundary layer. *J. Atmos. Oceanic Technol.*, **26**, 240–250, https://doi.org/10.1175/2008JTECHA1128.1.

Polkinghorne, R., and T. Vukicevic, 2011: Data assimilation of cloud-affected radiances in a cloud-resolving model. *Mon. Wea. Rev.*, **139**, 755–773, https://doi.org/10.1175/2010MWR3360.1.

Roberts, N. M., and H. W. Lean, 2008: Scale-selective verification of rainfall accumulations from high-resolution forecasts of convective events. *Mon. Wea. Rev.*, **136**, 78–97, https://doi.org/10.1175/2007MWR2123.1.

Romine, G. S., C. S. Schwartz, C. Snyder, J. L. Anderson, and M. L. Weisman, 2013: Model bias in a continuously cycled assimilation system and its influence on convection-permitting forecasts. *Mon. Wea. Rev.*, **141**, 1263–1284, https://doi.org/10.1175/MWR-D-12-00112.1.

Schwartz, C. S., 2016: Improving large-domain convection-allowing forecasts with high-resolution analyses and ensemble data assimilation. *Mon. Wea. Rev.*, **144**, 1777–1803, https://doi.org/10.1175/MWR-D-15-0286.1.

——, and Z. Liu, 2014: Convection-permitting forecasts initialized with continuously cycling limited-area 3DVAR, ensemble Kalman filter, and "hybrid" variational-ensemble data assimilation systems. *Mon. Wea. Rev.*, **142**, 716–738, https://doi.org/10.1175/MWR-D-13-00100.1.

——, and Coauthors, 2010: Toward improved convection-allowing ensembles: Model physics sensitivities and optimizing probabilistic guidance with small ensemble membership. *Wea. Forecasting*, **25**, 263–280, https://doi.org/10.1175/2009WAF2222267.1.

——, G. S. Romine, R. A. Sobash, K. R. Fossell, and M. L. Weisman, 2015: NCAR's experimental real-time convection-allowing ensemble prediction system. *Wea. Forecasting*, **30**, 1645–1654, https://doi.org/10.1175/WAF-D-15-0103.1.

Shao, H., and Coauthors, 2016: Bridging research to operations transitions: Status and plans of community GSI. *Bull. Amer. Meteor. Soc.*, **97**, 1427–1440, https://doi.org/10.1175/BAMS-D-13-00245.1.

Skamarock, W. C.,, and Coauthors, 2008: A description of the Advanced Research WRF version 3. NCAR Tech. Note NCAR/TN-475+STR, 113 pp., https://doi.org/10.5065/D68S4MVH.

Shun, C. M., and P. W. Chan, 2008: Applications of an infrared Doppler lidar in detection of wind shear. *J. Atmos. Oceanic Technol.*, **25**, 637–655, https://doi.org/10.1175/2007JTECHA1057.1.

Smith, T. M, and Coauthors, 2016: Multi-Radar Multi-Sensor (MRMS) severe weather and aviation products: Initial operating capabilities. *Bull. Amer. Meteor. Soc.*, **97**, 1617–1630, https://doi.org/10.1175/BAMS-D-14-00173.1.

Snook, N., M. Xue, and Y. Jung, 2011: Analysis of a tornadic mesoscale convective vortex based on ensemble Kalman filter assimilation of CASA X-band and WSR-88D radar data. *Mon. Wea. Rev.*, **139**, 3446–3468, https://doi.org/10.1175/MWR-D-10-05053.1.

Snyder, C., and F. Zhang, 2003: Assimilation of simulated Doppler radar observations with an ensemble Kalman filter. *Mon. Wea. Rev.*, **131**, 1663–1677, https://doi.org/10.1175//2555.1.

Sobash, R. A., and D. J. Stensrud, 2015: Assimilating surface mesonet observations with the EnKF to improve ensemble forecasts of convection initiation on 29 May 2012. *Mon. Wea. Rev.*, **143**, 3700–3725, https://doi.org/10.1175/MWR-D-14-00126.1.

——, and L. J. Wicker, 2015: On the impact of additive noise in storm-scale EnKF experiments. *Mon. Wea. Rev.*, **143**, 3067–3086, https://doi.org/10.1175/MWR-D-14-00323.1.

Stensrud, D. J., and Coauthors, 2013: Progress and challenges with Warn-on-Forecast. *Atmos. Res.*, **123**, 2–16, https://doi.org/10.1016/j.atmosres.2012.04.004.

——, N. Yussouf, D. C. Dowell, and M. C. Coniglio, 2009: Assimilating surface data into a mesoscale model ensemble: Cold pool analyses from spring 2007. *Atmos. Res.*, **93**, 207–220, https://doi.org/10.1016/j.atmosres.2008.10.009.

Stokes, G. M., and S. E. Schwartz, 1994: The Atmospheric Radiation Measurement (ARM) Program: Programmatic background and design of the cloud and radiation test bed. *Bull. Amer. Meteor. Soc.*, **75**, 1201–1221, https://doi.org/10.1175/1520-0477(1994)075<1201:TARMPP>2.0.CO;2.

Toth, Z., Y. Zhu, and R. Wobus, 2004: March 2004 upgrades of the NCEP global ensemble forecast system. NOAA/NCEP/EMC, accessed 28 June 2018, http://www.emc.ncep.noaa.gov/gmb/ens/ens_imp_news.html.

Turner, D., and W. G. Blumberg, 2019: Improvements to the AERIoe thermodynamic profile retrieval algorithm. *IEEE J. Sel. Topics Appl. Earth Obs. Remote Sens.*, **12**, 1339–1354, https://doi.org/10.1109/JSTARS.2018.2874968.

——, and U. Löhnert, 2014: Information content and uncertainties in thermodynamic profiles and liquid cloud properties retrieved from the ground-based Atmospheric Emitted Radiance Interferometer (AERI). *J. Appl. Meteor. Climatol.*, **53**, 752–771, https://doi.org/10.1175/JAMC-D-13-0126.1.

——, W. F. Feltz, and R. A. Ferrare, 2000: Continuous water vapor profiles from operational ground—Based active and passive remote sensors. *Bull. Amer. Meteor. Soc.*, **81**, 1301–1317, https://doi.org/10.1175/1520-0477(2000)081<1301:CWBPFO>2.3.CO;2.

——, E. J. Mlawer, and H. E. Revercomb, 2016: Water vapor observations in the ARM program. *The Atmospheric Radiation Measurement Program: The First 20 Years*, *Meteor. Monogr.*, No. 57, Amer. Meteor. Soc., 13.1–13.18, https://doi.org/10.1175/AMSMONOGRAPHS-D-15-0025.1.

Wagner, T. J., W. F. Feltz, and S. A. Ackerman, 2008: The temporal evolution of convective indices in storm-producing environments. *Wea. Forecasting*, **23**, 786–794, https://doi.org/10.1175/2008WAF2007046.1.

Wang, Y., and X. Wang, 2017: Direct assimilation of radar reflectivity without tangent linear and adjoint of the nonlinear observation operator in the GSI-based EnVar system: Methodology and experiment with the 8 May 2003 Oklahoma City tornadic supercell. *Mon. Wea. Rev.*, **145**, 1447–1471, https://doi.org/10.1175/MWR-D-16-0231.1.

Wang, X., D. Parrish, D. Kleist, and J. Whitaker, 2013: GSI 3DVar-based ensemble–variational hybrid data assimilation for NCEP Global Forecast System: Single-resolution experiments. *Mon. Wea. Rev.*, **141**, 4098–4117, https://doi.org/10.1175/MWR-D-12-00141.1.

Weckwerth, T. M., 2000: The effect of small-scale moisture variability on thunderstorm initiation. *Mon. Wea. Rev.*, **128**, 4017–4030, https://doi.org/10.1175/1520-0493(2000)129<4017:TEOSSM>2.0.CO;2.

——, and D. B. Parsons, 2006: A review of convection initiation and motivation for IHOP_2002. *Mon. Wea. Rev.*, **134**, 5–22, https://doi.org/10.1175/MWR3067.1.

Wei, M., Z. Toth, R. Wobus, and Y. Zhu, 2008: Initial perturbations based on the ensemble transform (ET) technique in the NCEP global operational forecast system. *Tellus*, **60A**, 62–79, https://doi.org/10.1111/j.1600-0870.2007.00273.x.

Wheatley, D. M., D. J. Stensrud, D. C. Dowell, and N. Yussouf, 2012: Application of a WRF mesoscale data assimilation system to springtime severe weather events 2007–09. *Mon. Wea. Rev.*, **140**, 1539–1557, https://doi.org/10.1175/MWR-D-11-00106.1.

——, K. H. Knopfmeier, T. A. Jones, and G. J. Creager, 2015: Storm-scale data assimilation and ensemble forecasting with the NSSL experimental Warn-on-Forecast system. Part I: Radar data experiments. *Wea. Forecasting*, **30**, 1795–1817, https://doi.org/10.1175/WAF-D-15-0043.1.

Whitaker, J. S., and T. M. Hamill, 2002: Ensemble data assimilation without perturbed observations. *Mon. Wea. Rev.*, **130**, 1913–1924, https://doi.org/10.1175/1520-0493(2002)130<1913:EDAWPO>2.0.CO;2.

——, and ——, 2012: Evaluating methods to account for system errors in ensemble data assimilation. *Mon. Wea. Rev.*, **140**, 3078–3089, https://doi.org/10.1175/MWR-D-11-00276.1.

——, ——, X. Wei, Y. Song, and Z. Toth, 2008: Ensemble data assimilation with the NCEP global forecast system. *Mon. Wea. Rev.*, **136**, 463–482, https://doi.org/10.1175/2007MWR2018.1.

Wu, W.-S., D. F. Parrish, E. Rogers, and Y. Lin, 2017: Regional ensemble–variational data assimilation using global ensemble forecasts. *Wea. Forecasting*, **32**, 83–96, https://doi.org/10.1175/WAF-D-16-0045.1.

Xue, M., and W. J. Martin, 2006: A high-resolution modeling study of the 24 May 2002 dryline case during IHOP. Part I: Numerical simulation and general evolution of the dryline and convection. *Mon. Wea. Rev.*, **134**, 149–171, https://doi.org/10.1175/MWR3071.1.

Yussouf, N., E. R. Mansell, L. J. Wicker, D. M. Wheatley, and D. J. Stensrud, 2013: The ensemble Kalman filter analyses and forecasts of the 8 May 2003 Oklahoma City tornadic supercell storm using single-and double-moment microphysics schemes. *Mon. Wea. Rev.*, **141**, 3388–3412, https://doi.org/10.1175/MWR-D-12-00237.1.

——, D. C. Dowell, L. J. Wicker, K. H. Knopfmeier, and D. M. Wheatley, 2015: Storm-scale data assimilation and ensemble forecasts for the 27 April 2011 severe weather outbreak in Alabama. *Mon. Wea. Rev.*, **143**, 3044–3066, https://doi.org/10.1175/MWR-D-14-00268.1.

——, J. S. Kain, and A. J. Clark, 2016: Short-term probabilistic forecasts of the 31 May 2013 Oklahoma tornado and flash flood event using a continuous-update-cycle storm-scale ensemble system. *Wea. Forecasting*, **31**, 957–983, https://doi.org/10.1175/WAF-D-15-0160.1.

Zhang, F., Z. Meng, and A. Aksoy, 2006: Tests of an ensemble Kalman filter for mesoscale and regional-scale data assimilation. Part I: Perfect model experiments. *Mon. Wea. Rev.*, **134**, 722–736, https://doi.org/10.1175/MWR3101.1.

Zhou, X., Y. Zhu, D. Hou, and D. Kleist, 2016: A comparison of perturbations from an ensemble transform and an ensemble Kalman filter for the NCEP Global Ensemble Forecast System. *Wea. Forecasting*, **31**, 2057–2074, https://doi.org/10.1175/WAF-D-16-0109.1.